nature neuroscience

ARTICLES

https://doi.org/10.1038/s41593-018-0296-9

Loss of TREM2 function increases amyloid seeding but reduces plaque-associated ApoE

Samira Parhizkar[1], Thomas Arzberger[2,3,4,5], Matthias Brendel[6], Gernot Kleinberger[1,2], Maximilian Deussing[6], Carola Focke[6], Brigitte Nuscher[1], Monica Xiong[7], Alireza Ghasemigharagoz[8], Natalie Katzmarski[9], Susanne Krasemann[10,11], Stefan F. Lichtenthaler[2,3,12,13], Stephan A. Müller[3,12], Alessio Colombo[3], Laura Sebastian Monasor[3], Sabina Tahirovic[3], Jochen Herms[2,3,4], Michael Willem[1], Nadine Pettkus[1], Oleg Butovsky[10,14], Peter Bartenstein[2,6], Dieter Edbauer[2,3], Axel Rominger[2,6,17], Ali Ertürk[8], Stefan A. Grathwohl[15], Jonas J. Neher[15,16], David M. Holtzman[7], Melanie Meyer-Luehmann[9*] and Christian Haass[1,2,3*]

Coding variants in the triggering receptor expressed on myeloid cells 2 (*TREM2*) are associated with late-onset Alzheimer's disease (AD). We demonstrate that amyloid plaque seeding is increased in the absence of functional Trem2. Increased seeding is accompanied by decreased microglial clustering around newly seeded plaques and reduced plaque-associated apolipoprotein E (ApoE). Reduced ApoE deposition in plaques is also observed in brains of AD patients carrying *TREM2* coding variants. Proteomic analyses and microglia depletion experiments revealed microglia as one origin of plaque-associated ApoE. Longitudinal amyloid small animal positron emission tomography demonstrates accelerated amyloidogenesis in *Trem2* loss-of-function mutants at early stages, which progressed at a lower rate with aging. These findings suggest that in the absence of functional Trem2, early amyloidogenesis is accelerated due to reduced phagocytic clearance of amyloid seeds despite reduced plaque-associated ApoE.

In many neurodegenerative disorders, misfolded amyloidogenic proteins propagate and spread throughout the brain in a characteristic manner reminiscent of prion-like disorders[1]. Seeding and spreading can be experimentally induced by intracerebral injection of homogenates derived from brains of humans with neurodegenerative disorders or respective mouse models[2]. Although little is known about the cellular mechanisms controlling and modifying prion-like propagation, it is conceivable that amyloid-β peptide (Aβ) clearance may be involved. Microgliosis has long been known as an overarching pathological phenomenon that is characteristic of almost all neurodegenerative disorders[3]. The recent identification of coding variants in genes that are selectively expressed in microglial cells and their genetic association with late-onset Alzheimer's disease (AD) and other neurodegenerative disorders, further pinpoint a pivotal disease-modifying role of microglia[4,5]. Among these microglial-expressed disease-associated genes, sequence variants in the gene encoding the triggering receptor expressed on myeloid cells 2 (*TREM2*) are associated with an extraordinarily increased risk for AD comparable to that conferred by the single apolipoprotein E (*APOE*) ε4 allele[6,7]. Trem2 is functionally required for a wide variety of important cellular functions, including chemotaxis[8], maintenance of energy metabolism[9,10], engulfment of dead cells[8] and phagocytosis of Aβ fibrils[11]. Recent findings have indicated that microglia switch from a homeostatic state to a neurodegenerative phenotype in several different disease models by suppressing their homeostatic messenger RNA profile and increasing a disease-associated transcriptional profile[12–14]. Trem2 and ApoE are both robustly upregulated in microglia responding to brain lesions[13,14]. Moreover, ApoE is a major constituent of amyloid plaques and ApoE promotes their aggregation and deposition[15–17]. Furthermore, anti-ApoE immunotherapy inhibits amyloid accumulation and deposition further supporting the role of ApoE in Aβ aggregation and clearance[18]. Conflicting data on the potential role of Trem2 in amyloid metabolism have been explained by the different model systems used, the

[1]Chair of Metabolic Biochemistry, Biomedical Center (BMC), Faculty of Medicine, Ludwig-Maximilians-Universität München, Munich, Germany. [2]Munich Cluster for Systems Neurology (SyNergy), Munich, Germany. [3]German Center for Neurodegenerative Diseases (DZNE) Munich, Munich, Germany. [4]Center for Neuropathology and Prion Research, Ludwig-Maximilians-Universität München, Munich, Germany. [5]Department of Psychiatry and Psychotherapy, Ludwig-Maximilians-Universität München, Munich, Germany. [6]Department of Nuclear Medicine, University Hospital, Ludwig-Maximilians-Universität München, Munich, Germany. [7]Department of Neurology, Hope Center for Neurological Disorders, and Charles F. and Joanne Knight Alzheimer's Disease Research Center, Washington University School of Medicine, St. Louis, MO, USA. [8]Institute for Stroke and Dementia Research, Klinikum der Universität München, Munich, Germany. [9]Department of Neurology, Medical Center University of Freiburg, and Faculty of Medicine, University of Freiburg, Freiburg, Germany. [10]Ann Romney Center for Neurologic Diseases, Department of Neurology, Brigham and Women´s Hospital, Harvard Medical School, Boston, MA, USA. [11]Institute of Neuropathology, University Medical Center Hamburg-Eppendorf, Hamburg, Germany. [12]Neuroproteomics, School of Medicine, Klinikum Rechts der Isar, Technische Universität München, Munich, Germany. [13]Institute for Advanced Study, Technische Universität München, Garching, Germany. [14]Evergrande Center for Immunologic Diseases, Brigham and Women's Hospital, Harvard Medical School, Boston, MA, USA. [15]Department of Cellular Neurology, Hertie Institute for Clinical Brain Research, University of Tübingen, Tübingen, Germany. [16]German Center for Neurodegenerative Diseases (DZNE) Tübingen, Tübingen, Germany. [17]Present address: Department of Nuclear Medicine, Inselspital, University Hospital Bern, Bern, Switzerland. *e-mail: melanie.meyer-luehmann@uniklinik-freiburg.de; christian.haass@mail03.med.uni-muenchen.de

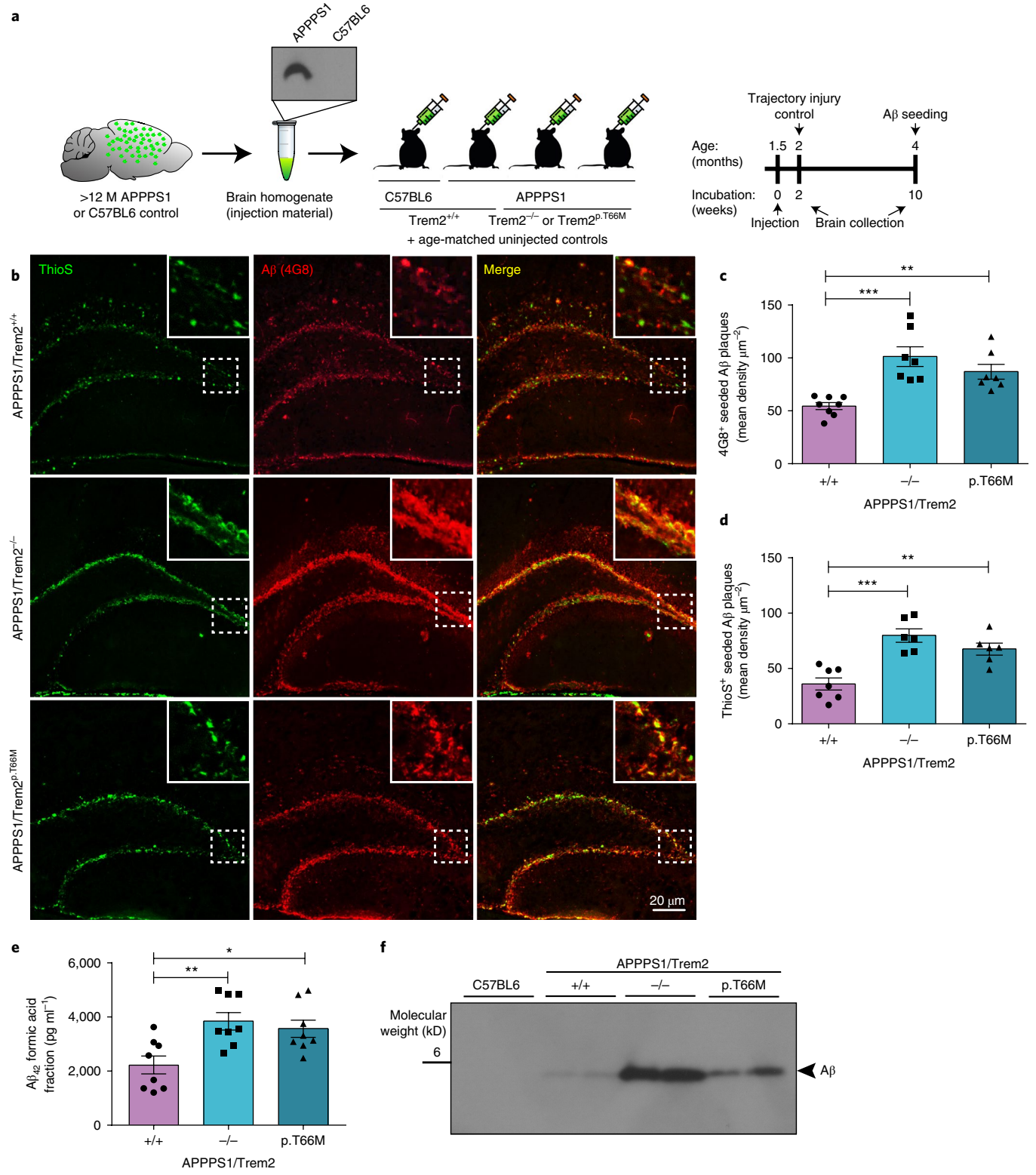

Fig. 1 | Increased amyloidogenesis on loss of Trem2 function. a, Schematic of the study design and timeline. **b**, In contrast to APPPS1/Trem2$^{+/+}$, Trem2 loss-of-function mice (APPPS1/Trem2$^{-/-}$ and APPPS1/Trem2$^{p.T66M}$) show increased amyloid seeding in the dentate gyrus at 4 months when injected with APPPS1 brain homogenates. Insets show seeding pathology at higher magnification as indicated by the area in dotted white box. **c**,**d**, Mice were analyzed for 4G8-positive immunoreactivity ($n^{+/+}=8$ mice, $n^{-/-}=7$ mice, $n^{p.T66M}=7$ mice; $F_{2,19}=13.13$, $P=0.0003$) (**c**) and ThioS-positive Aβ deposits ($n^{+/+}=7$ mice, $n^{-/-}=6$ mice, $n^{p.T66M}=6$ mice; $F_{2,16}=16.73$, $P=0.0001$) (**d**). **e**, $A\beta_{42}$ levels quantified in formic acid fractions using Meso Scale Discovery electrochemiluminescence assay confirm increased amyloid seeding in APPPS1/Trem2$^{-/-}$ and APPPS1/Trem2$^{p.T66M}$ mice compared with APPPS1/Trem2$^{+/+}$ mice ($n=8$ mice/genotype; $F_{2,21}=9.016$, $P=0.0015$). **f**, Immunoblotting with the anti-Aβ antibody 6E10 demonstrates increased Aβ in the formic acid fraction of APPPS1/Trem2$^{-/-}$ and APPPS1/Trem2$^{p.T66M}$ compared with APPPS1/Trem2$^{+/+}$ mice. Western blots were independently repeated five times to analyze $n=10$ mice/genotype. Full image of immunoblots are shown in Supplementary Fig. 7. Data represent mean ± s.e.m. One-way ANOVA, Dunnetts's post hoc analysis; $^{*}P<0.05$, $^{**}P<0.005$, $^{***}P<0.0005$.

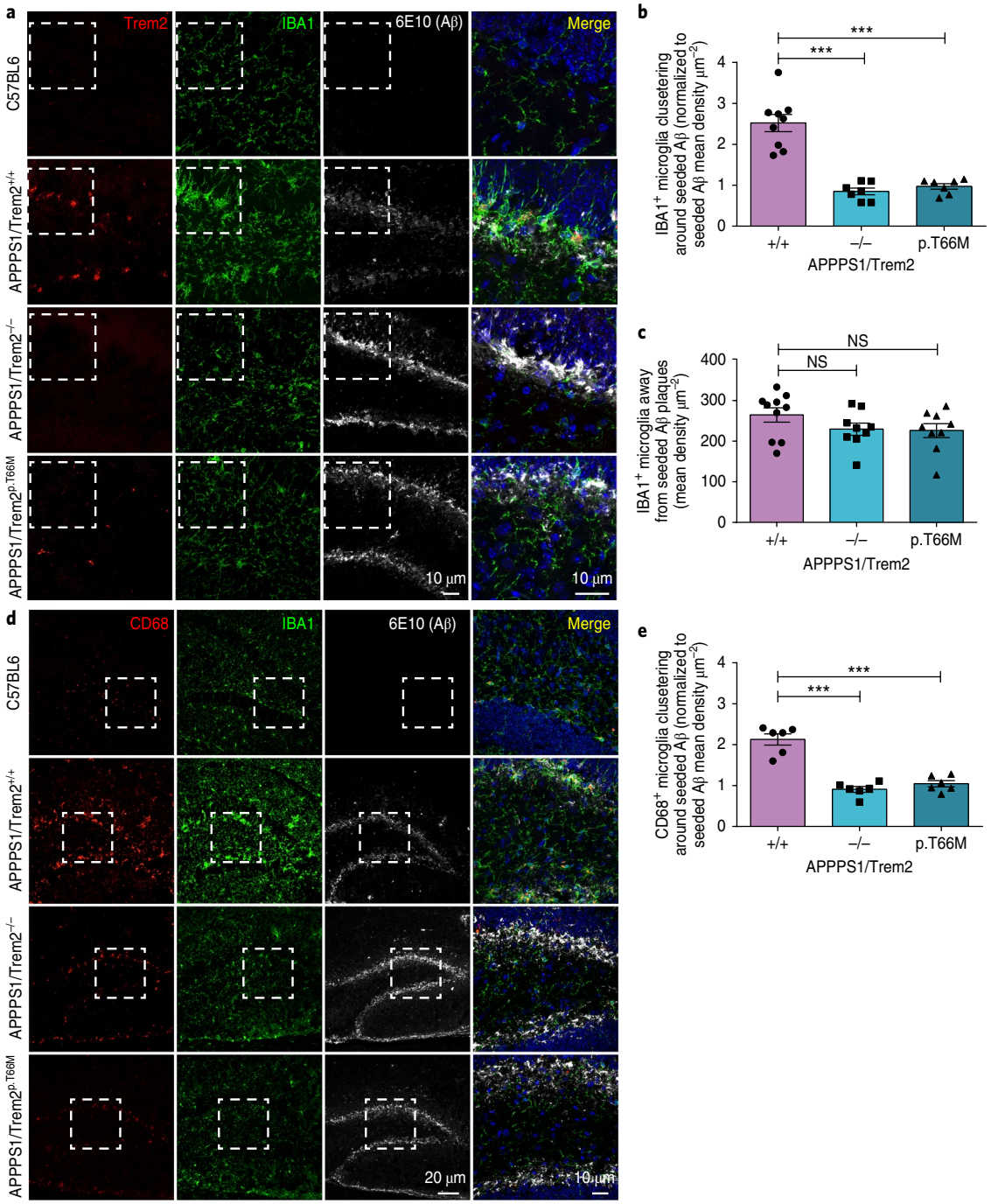

Fig. 2 | Reduced microglial clustering, CD68, and Trem2 expression in microglia around newly seeded plaques in Trem2 loss-of-function mice. a, First row: random distribution of IBA1-positive microglia in C57BL6 mice. Second row: clustering of IBA1 and Trem2-positive microglia around seeded plaques in the hippocampus of APPPS1/Trem2$^{+/+}$ mice. Third and fourth rows: loss of Trem2 function reduces microglia clustering around seeded plaques. **b**, IBA1-positive microglia clustering around seeded amyloid plaques ($n^{+/+}=9$ mice, $n^{-/-}=7$ mice, $n^{p.T66M}=7$ mice, $F_{2,20}=38.87$, $P=1.5\times10^{-7}$) normalized to seeded amyloid pathology shown in Fig. 1c. **c**, IBA1 immunoreactivity quantified in the hippocampus excluding seeded dentate gyrus ($n^{+/+}=10$ mice, $n^{-/-}=9$ mice, $n^{p.T66M}=9$ mice, $F_{2,25}=1.657$, $P=0.2109$). **d**, First row: CD68 expression is at the detection limit in C57BL6 mice. Second row: increased CD68 staining in IBA1-positive microglia around seeded plaques in the presence of functional Trem2. Third and fourth rows: reduced CD68 expression in microglia around seeded plaques in the absence of functional Trem2. **e**, Quantification of CD68-positive microglia in the seeded dentate gyrus ($n=6$ mice/genotype, $F_{2,15}=44.87$, $P=4.6\times10^{-7}$) normalized to seeded amyloid pathology shown in Fig. 1a. Dotted white boxes indicate the area in each staining that is merged and shown at higher magnification. Data represent mean ± s.e.m. One-way ANOVA, Dunnett's post hoc analysis; NS, not significant; $P>0.05$; ***$P<0.0005$.

stage of neuropathology, and the artificially increased production and rapid deposition of Aβ in transgenic mouse models highly overexpressing the amyloid precursor protein (APP) along with autosomal dominant APP and presenilin (PSEN) mutations[5,19–22]. To elucidate the role of Trem2 at the earliest accessible time point in the amyloid cascade, we used an in vivo seeding paradigm and performed intrahippocampal injections of Aβ-containing brain extracts into APPPS1 transgenic mice that previously have been

shown to robustly induce Aβ plaque formation in vivo[2]. By additionally analyzing non-experimentally seeded cortical Aβ plaques, we could directly compare the effect of Trem2 on more mature plaques within the same mice. Furthermore, we used longitudinal small animal positron emission tomography (μPET) imaging to monitor microglial activation and the kinetics of amyloid deposition up to an age of 12 months. Finally, we investigated microglial clustering and ApoE deposition in amyloid plaques in loss-of-Trem2-function mice as well as in AD cases with *TREM2* coding variants.

Results

Increased amyloid plaque seeding in the absence of functional Trem2. Amyloid plaques can be induced experimentally in vivo by a prion-like mechanism via inoculation of Aβ-containing homogenates in transgenic mice. Intracerebral injection of Aβ-rich brain extracts from AD patients or from aged APP transgenic mice promotes early formation and seeding of plaques[2,23]. Compared with non-experimentally seeded APP transgenic mice, the seeding model provides the unique opportunity to study plaque formation within a very defined and early time window with minimal variation from one mouse to another[2,23]. In contrast, uninjected non-seeded APP mice do not develop any seeded plaques and have an unpredictable onset of plaque formation at young age. Therefore, to examine the very early effects of loss of Trem2 function on the premature formation of Aβ plaques as well as on the capacity of microglia to remove Aβ seeds, we stereotactically injected brain homogenates derived from APP transgenic mice expressing $APP^{695KM670/671NL}$ and $PSEN1^{L166P}$ (APPPS1 mice)[24] into hippocampi of six-week-old APPPS1/Trem2$^{+/+}$, APPPS1/Trem2$^{-/-}$(ref. [25]), or APPPS1/$Trem2^{p.T66M}$ (ref. [10]) mice as well as non-transgenic C57BL6 littermates (Fig. 1a and Supplementary Fig. 1a). Ten weeks later, at a time point when normally little to no plaques are observed within the hippocampus (Supplementary Fig. 1a,b)[2], mice were killed and brains were prepared for immunohistochemistry and protein analysis. No seeded plaques were observed within the hippocampi of non-transgenic C57BL6 mice (Supplementary Fig. 1a,b), two weeks post-injection controls (Supplementary Fig. 1c), or uninjected APPPS1/Trem2$^{+/+}$, APPPS1/Trem2$^{-/-}$, or APPPS1/$Trem2^{p.T66M}$ mice (Supplementary Fig. 1d). In contrast, intense amyloid plaque seeding was observed in the subgranular layer of the hippocampi of APPPS1/Trem2$^{+/+}$ mice on injection of Aβ-containing brain homogenates as previously published[2,23] (Fig. 1b and Supplementary Fig. 1a,b). No seeding was observed on injection of lysates from Aβ-free C57BL6 mice (Supplementary Fig. 1a,b). As previously described by Meyer-Luehmann et al.[2], seeded amyloid plaques had a coarse and punctate appearance (Fig. 1b and Supplementary Fig. 1a) in the presence of Trem2. In contrast, in the absence of Trem2, the area occupied by seeded amyloid plaques not only increased (Fig. 1b), but also showed a more diffuse 4G8 staining as well as less separation of individual thioflavine S (ThioS)-positive fibrillar Aβ puncta (Fig. 1b). While all seeded amyloid plaques were detected immunopositively by 4G8 antibody, ThioS stained the dense cored plaques only. Although the T66M mutation has been strongly linked to Nasu–Hakola disease and frontotemporal dementia-like syndrome rather than AD[26], we used the APPPS1/$Trem2^{p.T66M}$ model to investigate Trem2-dependent microglial effects on amyloid seeding in a second independent loss-of-function model[10,11]. Similar findings were obtained when we injected Aβ-containing brain homogenates in hippocampi of APPPS1 mice endogenously expressing the $Trem2^{p.T66M}$ loss-of-function mutation (APPPS1/$Trem2^{p.T66M}$)[10] (Fig. 1b). Quantitative image analysis, $Aβ_{42}$ enzyme-linked immunosorbent assay (ELISA), as well as western blotting confirmed increased amyloidogenesis in the absence of functional Trem2 (Fig. 1c–f). These findings show that Trem2-dependent microglial functions limit early amyloidogenesis.

Reduced microglial clustering around seeded plaques in the absence of functional Trem2. Since chemotaxis and plaque association of microglia is disturbed on loss of Trem2 function[8,20,27], we next investigated clustering of microglia around newly seeded plaques. In C57BL6 control mice injected with APPPS1 mouse brain homogenate, microglia were randomly distributed throughout the hippocampus and microglial Trem2 expression was below the detection limit (Fig. 2a). In contrast, microglia clustered around seeded plaques on injection of Aβ-containing brain homogenates into APPPS1/Trem2$^{+/+}$ mice and increased Trem2 expression (Fig. 2a). Moreover, microglia clustering was severely reduced in APPPS1/Trem2$^{-/-}$ or APPPS1/$Trem2^{p.T66M}$ mice (Fig. 2a,b), although the density of ionized calcium-binding adaptor molecule 1 (IBA1)-positive microglia outside the seeded plaque-laden dentate gyrus was not significantly different (Fig. 2c). Clustering of microglia around seeded plaques was accompanied by increased CD68 staining, a marker for lysosomal activity, which was significantly reduced in APPPS1/Trem2$^{-/-}$ or APPPS1/$Trem2^{p.T66M}$ mice (Fig. 2d,e). Contrary to Trem2 loss-of-function mice, intracellular 6E10-positive Aβ staining was observed in plaque-associated IBA1, Trem2, and CD68-positive microglia in APPPS1/Trem2$^{+/+}$ mice, indicating microglial engulfment and phagocytosis of amyloid plaques (Fig. 2a,d).

In line with previous data[9,19,20], microglia also clustered around non-experimentally seeded cortical Aβ plaques (Supplementary Fig. 2a,b), and exhibited a robust increase of Trem2 (Supplementary Fig. 2a) and CD68 expression (Supplementary Fig. 2c). Again,

Fig. 3 | Increased amyloidogenesis in young Trem2 deficient mice is followed by lower amyloid accumulation rates during aging. a, Cortical microglial activity measured by in vivo TSPO μPET at ages of 3 ($P = 0.418$), 6 ($P = 0.426$), and 12 months ($P = 0.002$) for Trem2-deficient APPPS1 mice compared with APPPS1/Trem2$^{+/+}$. Age-matched results for C57BL6 mice with and without Trem2 deficiency are implemented for comparison with mice lacking amyloid pathology. **b**, Corresponding results for cortical fibrillar amyloidogensis assessed by in vivo amyloid μPET at 3 ($P = 0.026$), 6 ($P = 0.007$), and 12 months ($P = 0.895$). (APPPS1: 3 months Aβ PET $n^{+/+} = 4$ mice, TSPO PET $n^{+/+} = 5$ mice, Aβ PET $n^{-/-} = 7$ mice, TSPO PET $n^{-/-} = 9$ mice; 6 months Aβ PET $n^{+/+} = 12$ mice, TSPO PET $n^{+/+} = 13$ mice, Aβ PET $n^{-/-} = 9$ mice, TSPO PET $n^{-/-} = 11$ mice; 12 months Aβ PET $n^{+/+} = 11$ mice, TSPO PET $n^{+/+} = 11$ mice, Aβ PET $n^{-/-} = 7$ mice, TSPO PET $n^{-/-} = 7$ mice. C57BL6: 3 months Aβ PET $n^{+/+} = 6$ mice, TSPO PET $n^{+/+} = 6$ mice, Aβ PET $n^{-/-} = 5$ mice, TSPO PET $n^{-/-} = 6$ mice; 6 months Aβ PET $n^{+/+} = 25$ mice, TSPO PET $n^{+/+} = 20$ mice, Aβ PET $n^{-/-} = 6$ mice, TSPO PET $n^{-/-} = 8$ mice; 12 months Aβ PET $n^{+/+} = 21$ mice, TSPO PET $n^{+/+} = 20$ mice, Aβ PET $n^{-/-} = 7$ mice, TSPO PET $n^{-/-} = 7$ mice). $SUVR_{WM}$, standardized uptake value ratio to white matter. Error bars represent mean ± s.d. Two-sided *t* test. **c**, Coronal and axial slices show *Z*-scores of increased TSPO μPET against age-matched C57BL6 ($n = 18$ mice) to compare APPPS1/Trem2$^{-/-}$ and APPPS1/Trem2$^{+/+}$ at 3, 6, and 12 months of age using an MRI template. **d**, Coronal and axial slices show *Z*-scores of increased amyloid μPET against age-matched C57BL6 ($n = 18$ mice) to compare APPPS1/Trem2$^{-/-}$ and APPPS1/Trem2$^{+/+}$ at 3, 6, and 12 months. **e**, Serial imaging shows distinctly lower monthly increases for TSPO μPET during aging (6–12 months) in APPPS1/Trem2$^{-/-}$ mice compared with APPPS1/Trem2$^{+/+}$ mice ($n^{+/+} = 11$ mice, $n^{-/-} = 11$ mice, 3–5 months $P = 0.756$, 6–8 months $P = 8.03 \times 10^{-7}$, 9–11 months $P = 0.003$). **f**, Serial amyloid μPET indicates an increased accumulation rate of fibrillar amyloidogenesis in young APPPS1/Trem2$^{-/-}$ mice (3–5 months) compared with age-matched APPPS1/Trem2$^{+/+}$ mice. Notably, the accumulation rate of fibrillar amyloid in APPPS1/Trem2$^{-/-}$ mice declines below those of APPPS1/Trem2$^{+/+}$ during aging (6–12 months) $n^{+/+} = 10$ mice, $n^{-/-} = 9$ mice, 3–5 months $P = 1.52 \times 10^{-4}$, 6–8 months $P = 0.003$, 9–11 months $P = 1.48 \times 10^{-4}$). Thick lines in **e** and **f** represent polynomic functions of longitudinal changes, whereas dotted lines represent functions of s.e.m. Two-sided *t* test. NS, $P > 0.05$; $^{*}P < 0.05$; $^{**}P < 0.01$; $^{***}P < 0.001$.

clustering of microglia as well as CD68 expression were both reduced in Trem2 loss-of-function mice (Supplementary Fig. 2a–d), whereas the density of IBA1-positive microglia in a non-plaque bearing area such as the thalamic nuclei was not significantly different (Supplementary Fig. 2e).

Loss of Trem2 function changes the kinetics of amyloidogenesis. Conventional immunohistochemical analyses of brain-region-specific amyloid plaque burden in Trem2-deficient APP transgenic mice at different ages have yielded conflicting results[5,19–22]. Therefore, to longitudinally investigate whether amyloid plaque accumulation is affected by Trem2 loss of function during disease development in the entire brain, we performed dual-tracer longitudinal μPET imaging using tracers for amyloidogenesis (florbetaben) and microglia activation (translocator protein; TSPO)[28] (Fig. 3 and Supplementary Fig. 3). APPPS1 as well as C57BL6 mice with and

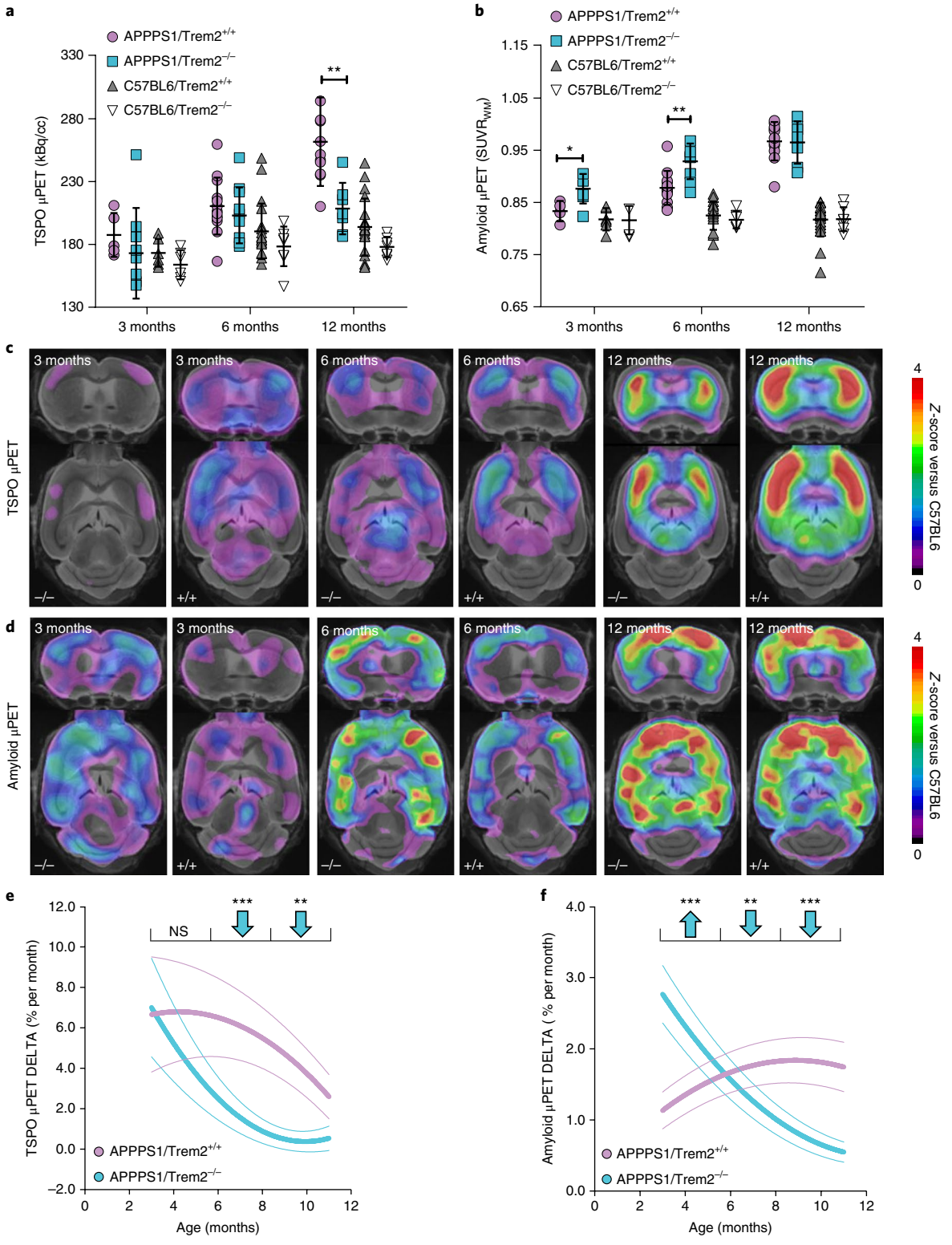

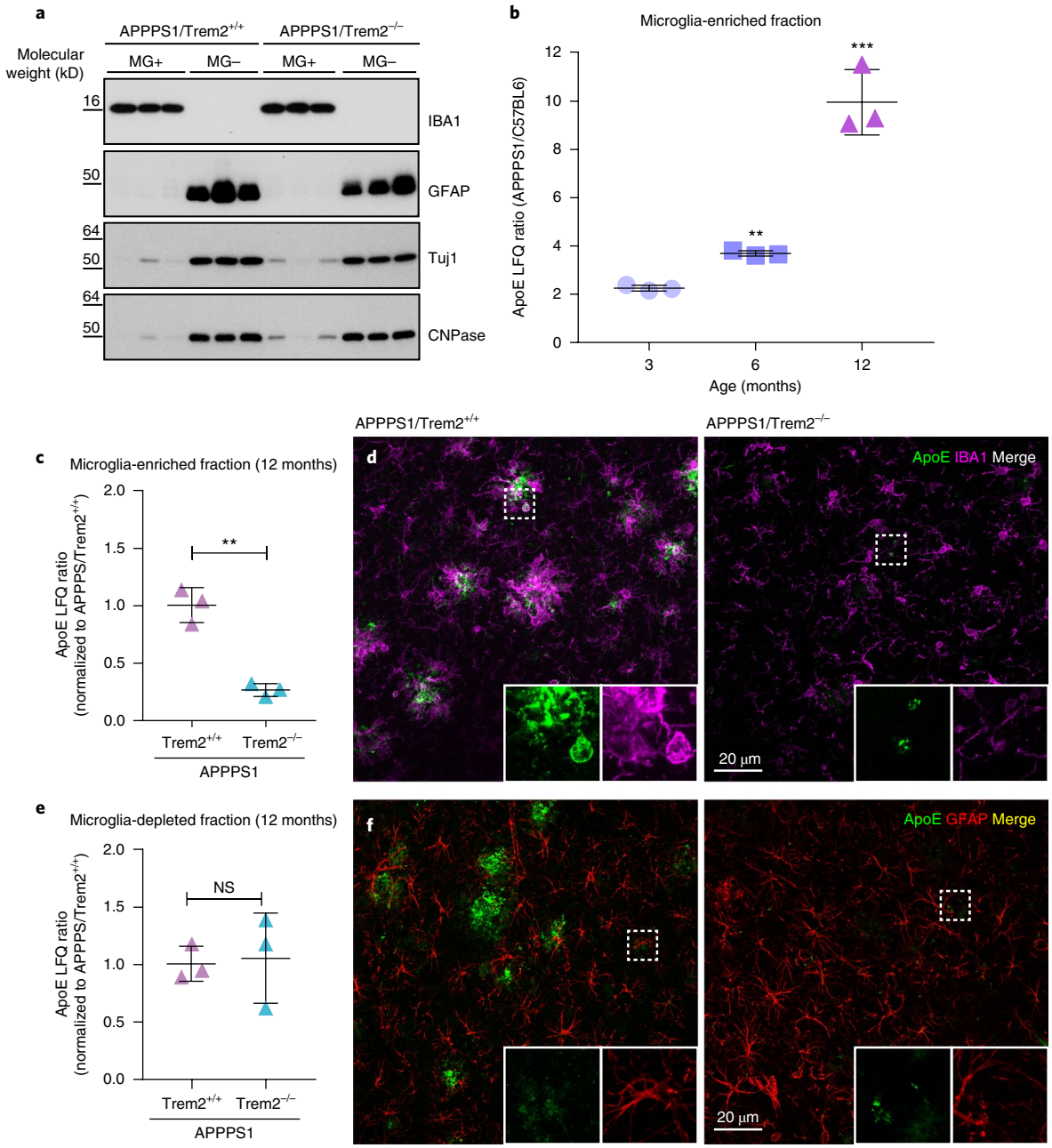

Fig. 4 | Relative protein quantification of ApoE in microglia-enriched and microglia-depleted lysates using mass spectrometry and label-free quantification (LFQ). a, Immunoblotting of microglia-enriched (MG^+) and microglia-depleted (MG^-) lysates from 12-month-old APPPS1/Trem2$^{+/+}$ and APPPS1/Trem2$^{-/-}$ mice. Brain cell types in each fraction were identified by detection of IBA1 for microglia, GFAP for astrocytes, neuron-specific Class III β-tubulin (Tuj1) for neurons, and 2′,3′-cyclic nucleotide 3′-phosphodiesterase (CNPase) for oligodendrocytes. Full image of each immunoblot is shown in Supplementary Fig. 7. **b**, ApoE LFQ intensities of microglia-enriched lysates in APPPS1/Trem2$^{+/+}$ mice compared with age-matched C57BL6 controls. Two-sided Student's *t* test comparing $\log_2$-transformed LFQ intensities of APPPS1 ($n=3$ mice) and C57BL6 ($n=3$ mice) separately for 3 ($P=0.061$), 6 ($P=0.00372$), and 12 months ($P=1.78\times10^{-5}$) of age (**$P<0.01$; ***$P<0.001$). **c**, ApoE LFQ intensities of microglia-enriched lysates from 12-month-old APPPS1/Trem2$^{-/-}$ mice show significantly reduced ApoE compared with age-matched APPPS1/Trem2$^{-/-}$ controls ($n=3$ mice/genotype). APPPS1 mice show significant reduction in ApoE after loss of Trem2 ($P=0.00105$). **d**, ApoE and IBA1 co-stained in 12-month-old APPPS1/Trem2$^{+/+}$ and APPPS1/Trem2$^{-/-}$ mice. White boxes indicate the area in each staining that is magnified as inset. **e**, Microglia-depleted lysates from 12-month-old APPPS1 mice show no statistically significant changes regardless of Trem2 expression ($n=3$ mice/genotype; $P=0.979$). Data represent mean ± s.d. **f**, ApoE and GFAP co-stained in 12-month-old APPPS1/Trem2$^{+/+}$ and APPPS1/Trem2$^{-/-}$ mice. White boxes indicate the area in each staining that is magnified as inset.

without Trem2 expression were subjected to µPET imaging from 3 to 12 months of age. Both µPET tracers demonstrated their feasibility to track changes over time in individual mice (Supplementary Fig. 3a–d). However, due to limited resolution, µPET was not appropriate for in vivo assessment of small hippocampal plaques in the seeding model. Additionally, individual µPET data of each imaging time point were validated by corresponding immunohistochemistry, which gave strong correlations between X-34 staining and the amyloid µPET signal as well as between CD68 staining and the TSPO µPET signal (Supplementary Fig. 3e–l).

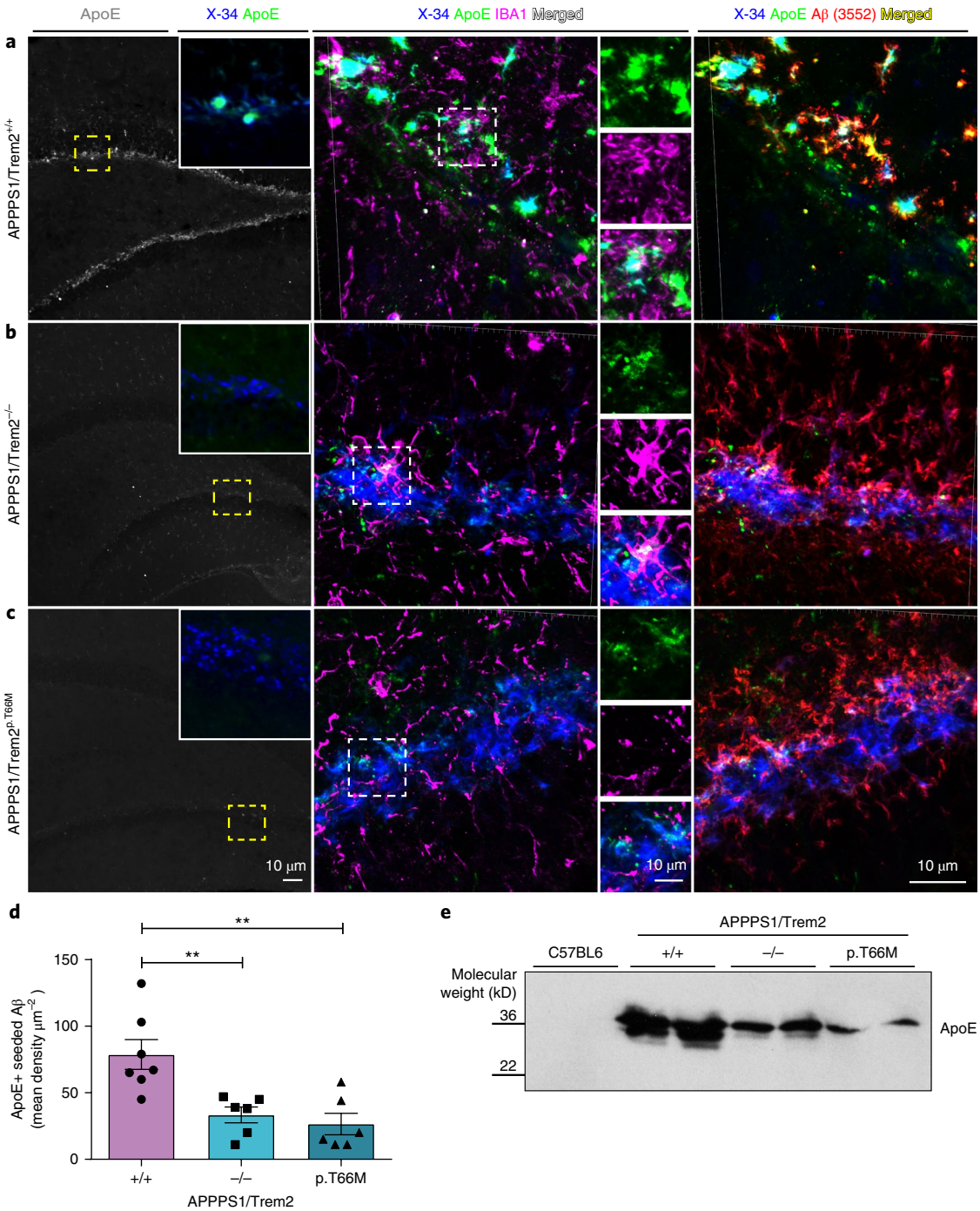

Fig. 5 | Decreased ApoE in newly seeded hippocampal plaques in the absence of functional Trem2. a, Left: ApoE (gray) staining in seeded hippocampus of APPPS1/Trem2$^{+/+}$ mice. Inset shows a higher magnification of ApoE (green) colocalized with X-34-positive seeded plaques (blue) in the same area shown in yellow dotted box. Middle: 3D reconstructed images of X-34/ApoE/IBA1 stainings of seeded area in APPPS1/Trem2$^{+/+}$ dentate gyrus. Enlarged areas of each staining (top, ApoE in green; middle, IBA1 in magenta; bottom, merged in white) are shown adjacently. Right: 3D reconstructed images of X-34/ApoE/Aβ (3552) stainings of seeded area in APPPS1/Trem2$^{+/+}$ dentate gyrus. **b**,**c**, Left: reduced ApoE staining (gray) in seeded APPPS1/Trem2$^{-/-}$ mice (**b**) and APPPS1/Trem2$^{p.T66M}$ mice (**c**) compared with APPPS1/Trem2$^{+/+}$ mice. Insets show a higher magnification of ApoE (green) with seeded amyloid pathology (X-34; blue) in the same area indicated in yellow dotted box. Middle: reconstructed images of X-34/ApoE/IBA1 show reduced IBA1 and ApoE colocalization in APPPS1/Trem2$^{-/-}$ mice (**b**) and APPPS1/Trem2$^{p.T66M}$ mice (**c**). Right: 3D reconstructed images of x34/ApoE/Aβ (3552) stainings of seeded area in APPPS1/Trem2$^{-/-}$ (**b**) and APPPS1/Trem2$^{p.T66M}$ (**c**) dentate gyrus show increased amyloid pathology despite reduced ApoE levels. Note increased staining of non-fibrillar (X-34-negative) Aβ on Trem2 loss of function in **b** and **c** compared with **a**. **d**, Quantification of mean ApoE density over seeded amyloid pathology area ($n^{+/+}=7$ mice, $n^{-/-}=6$ mice, $n^{p.T66M}=6$ mice; $F_{2,16}=10.35$, $P=0.0013$). **e**, Immunoblotting with the anti-ApoE antibody HJ6.3 demonstrates decreased hippocampal ApoE in the formic acid fraction of seeded APPPS1/Trem2$^{-/-}$ and APPPS1/Trem2$^{p.T66M}$ compared with APPPS1/Trem2$^{+/+}$ mice. Western blots were independently repeated three times to analyze $n=6$ mice/genotype. Full image of immunoblots are shown in Supplementary Fig. 7. Data represent mean ± s.e.m. One-way ANOVA, Dunnett's post hoc analysis; $^{**}P<0.005$.

As expected, microglial activation was highly increased in APPPS1/Trem2$^{+/+}$ mice at 12 months compared with age-matched C57BL6 mice without amyloidogenesis (Fig. 3a,c). Trem2 loss-of-function APPPS1 mice mainly displayed a reduced ability of microglial activation at 12 months of age when compared with age-matched APPPS1/Trem2$^{+/+}$ (Fig. 3a,c). Importantly, we observed a significantly reduced longitudinal progression of microglial activity (Fig. 3e and Supplementary Fig. 3a,c) from 3 to 12 months of age in APPPS1/Trem2$^{-/-}$ compared with APPPS1/Trem2$^{+/+}$ mice. Increased microglial activation in APPPS1/Trem2$^{+/+}$ compared with APPPS1/Trem2$^{-/-}$ or C57BL6 mice reflected the previously observed high ^{18}[F]-GE180 uptake in microglial cells and low retention in the non-inflamed and non-diseased brain[29].

Interestingly, amyloid μPET imaging revealed an increased fibrillar amyloidogenesis early during pathogenesis in APPPS1/Trem2$^{-/-}$ mice at 3 and 6 months, which leveled out during late disease progression at 12 months of age (Fig. 3b,d). Noteworthy, fibrillar amyloidogenesis was already significantly elevated in 3-month-old APPPS1/Trem2$^{-/-}$ compared with age-matched APPPS1/Trem2$^{+/+}$ mice. Furthermore, we observed a significantly lower accumulation rate of fibrillar amyloid from 6 to 12 months of age (Fig. 3f and Supplementary Fig. 3b,d). In contrast, monthly rates of fibrillar amyloid accumulation were elevated in APPPS1/Trem2$^{-/-}$ compared with APPPS1/Trem2$^{+/+}$ mice between 3 and 6 months of age (Fig. 3f). This suggests an initial phase of enhanced fibrillar amyloidogenesis is followed by a later phase of slower amyloid deposition or alternatively, an earlier saturation of amyloid deposition in *Trem2* knockout mice as a result of an elevated baseline. Regardless of the mechanism involved, this may suggest that additional age-dependent factors contribute to plaque growth and clearance during disease progression.

ApoE load of amyloid plaques depends on functional Trem2. Since disease-associated microglia migrate toward amyloid plaques and increase ApoE mRNA[13,14,30], we wondered whether ApoE-expressing microglia might directly contribute to the ApoE load of amyloid deposits and therefore could contribute to the observed changes in the kinetics of amyloid plaque deposition. To find out whether microglia or astrocytes and other neuronal cells selectively contribute to the entire pool of ApoE, we first compared ApoE protein abundance in lysates from microglia-enriched and microglia-depleted fractions obtained from 12-month-old APPPS1 mice in the presence or absence of Trem2. Enrichment of microglia as well as depletion of microglia was confirmed in the corresponding fractions by western blotting with antibodies to microglial, astroglial, neuronal, and oligodendrocytic marker proteins (Fig. 4a). Protein abundance of ApoE in microglia-enriched fractions increased from 3 to 12 months in APPPS1/Trem2$^{+/+}$ mice (Fig. 4b). Moreover, proteomic analysis of APPPS1/Trem2$^{+/+}$ mice revealed increased ApoE abundance selectively in the microglia-enriched fraction when compared with APPPS1/Trem2$^{-/-}$ mice (Fig. 4c). Increased production of ApoE in microglia was further confirmed by ApoE/IBA1 co-stainings (Fig. 4d). In contrast, the microglia-depleted fraction showed no Trem2-dependent change in ApoE production (Fig. 4e), which was also confirmed by immunohistochemistry (Fig. 4f). This suggests that microglia may be directly involved in the process of ApoE co-deposition in amyloid plaques, since the strong increase of microglial ApoE expression occurs only when microglia switch to the disease-associated signature on clustering around amyloid plaques[13,14]. We therefore investigated deposition of ApoE in newly seeded amyloid plaques in the presence and absence of Trem2-dependent microglial clustering. Seeded plaques within the hippocampus were robustly co-stained with ApoE in APPPS1/Trem2$^{+/+}$ mice (Fig. 5a). In contrast, on loss of Trem2 function, newly seeded hippocampal plaques showed a significant reduction of plaque-associated ApoE (Fig. 5b–d) despite higher plaque load. Reduced plaque-associated ApoE was confirmed by western blotting of plaque-enriched formic acid hippocampal extracts (Fig. 5e). Similar findings were obtained when we investigated non-experimentally seeded cortical Aβ plaques in the same mice (Fig. 6). Again, while APPPS1/Trem2$^{+/+}$ mice showed robust ApoE association with amyloid plaques (Fig. 6a), the ApoE load in cortical plaques of APPPS1/Trem2$^{-/-}$ or APPPS1/Trem2$^{p.T66M}$ mice was significantly reduced (Fig. 6b–e). Similarly, co-immunostaining of ApoE and IBA1-positive microglia was significantly lower on loss of Trem2 function compared with APPPS1/Trem2$^{+/+}$ mice (Fig. 6f). This is in line with both the absence of ApoE mRNA induction in microglia on loss of Trem2 function[8,14], and the age-dependent increase in ApoE protein levels in microglia from APPPS1/Trem2$^{+/+}$ mice (Fig. 4b). Indeed, in APPPS1/Trem2$^{+/+}$ mice, microglia clustering around seeded plaques within the hippocampus (Fig. 5a) or around non-experimentally seeded cortical Aβ plaques (Fig. 6a) express enhanced levels of ApoE in contrast to microglia in Trem2 loss-of-function mice as shown by three-dimensional (3D) reconstruction of high-resolution confocal images (Figs. 5b–e and 6b–f). Thus, loss of Trem2 function leads to a rather dramatic reduction of ApoE co-deposition in amyloid plaques.

To independently verify microglia as one source of amyloid plaque-associated ApoE, we investigated ApoE co-deposition in amyloid plaques in brains of microglia-depleted APPPS1 mice (Fig. 7). APPPS1 mice crossed to mice expressing thymidine kinase of herpes simplex virus (TK) under the CD11b promoter were used for this study[31]. *TK* as a suicide gene converts antiviral nucleotide analog prodrugs such as ganciclovir (GCV) into a monophoshorylated form, which is subsequently transformed into a toxic triphosphate variant by cellular kinases. GCV treatment for longer than three weeks can lead to microhemorrhages in the brain as well as increased rate of lethality[31]. With these limitations

Fig. 6 | Decreased ApoE in non-experimentally seeded cortical Aβ plaques after loss of Trem2 function. a, Left: ApoE (gray) staining of non-experimentally seeded cortical Aβ plaques of APPPS1/Trem2$^{+/+}$ mice. Inset demonstrates a higher magnification of ApoE (green) colocalized with X-34-positive cortical plaque (blue) in the same area shown in yellow dotted box. Middle: high-resolution confocal images of X-34/ApoE/IBA1 stained cortical amyloid plaque in APPPS1/Trem2$^{+/+}$ were 3D reconstructed. Selected areas of each staining (top, ApoE in green; middle, IBA1 in magenta; bottom, merged in white) are shown adjacently. Right: 3D reconstructed high-resolution confocal images of X-34/ApoE/Aβ (3552) stained amyloid plaque in APPPS1/Trem2$^{+/+}$ cortex. Immunopositive Aβ (red) and ApoE (green) are strongly colocalized (yellow). **b**,**c**, Left: reduced ApoE staining (gray) in cortical amyloid plaques of APPPS1/Trem2$^{-/-}$ mice (**b**) and APPPS1/Trem2$^{p.T66M}$ mice (**c**). Dotted cyan box indicates the area that is magnified as inset (ApoE, green; X-34, blue). Middle: 3D reconstructed images of X-34/ApoE/IBA1 show reduced IBA1 and ApoE colocalization in APPPS1/Trem2$^{-/-}$ mice (**b**) and APPPS1/Trem2$^{p.T66M}$ mice (**c**). Right: 3D reconstructed images of X-34/ApoE/Aβ (3552) stained amyloid plaque in APPPS1/Trem2$^{-/-}$ (**b**) and APPPS1/Trem2$^{p.T66M}$ (**c**) cortex show very little to no colocalization between ApoE (green) and immunopositive Aβ (red). **d**, Immunoblotting with the anti-ApoE antibody HJ6.3 shows decreased cortical ApoE in the formic acid fraction of seeded APPPS1/Trem2$^{-/-}$ and APPPS1/Trem2$^{p.T66M}$ compared with APPPS1/Trem2$^{+/+}$ mice. Western blots were independently repeated four times to analyze at least $n=8$ mice/genotype. Full image of immunoblots are shown in Supplementary Fig. 7. **e**, Quantification of ApoE density in cortex ($n=5$ mice/genotype; $F_{2,12}=14.31$, $P=0.0007$). **f**, Quantification of ApoE colocalization in IBA1-positive microglia in APPPS1/Trem2$^{+/+}$, APPPS1/Trem2$^{-/-}$, and APPPS1/Trem2$^{p.T66M}$ mice ($n=5$ mice/genotype; $F_{2,12}=18.82$, $P=0.0002$). Data represent mean ± s.e.m. One-way ANOVA, Dunnett's post hoc analysis; $^{**}P<0.005$.

in mind, we decided to include 3-month-old APPPS1/TK+ mice treated with GCV for two weeks only to avoid side effects (Fig. 7a). Moreover, the subsequent two weeks during which no GCV was administered allowed repopulation of the brain parenchyma with peripheral monocytes, which failed to cluster around plaques[32]. Compared with APPPS1/TK– controls, immunohistochemical analyses demonstrated significantly reduced plaque-associated ApoE on microglial depletion (Fig. 7b–f and Supplementary Fig. 4a). Moreover, newly re-populated IBA1-positive cells in APPPS1/TK+ mice displayed decreased IBA1/ApoE co-staining (Fig. 7d,g and Supplementary Fig. 4b). In contrast to microglia, glial fibrillary acidic protein (GFAP)-positive astrocytic staining in both APPPS1/TK mice showed no changes in GFAP/ApoE co-localization (Fig. 7e,g and Supplementary Fig. 4c). These findings provide further evidence for the pivotal role of microglia as one source of plaque-associated ApoE.

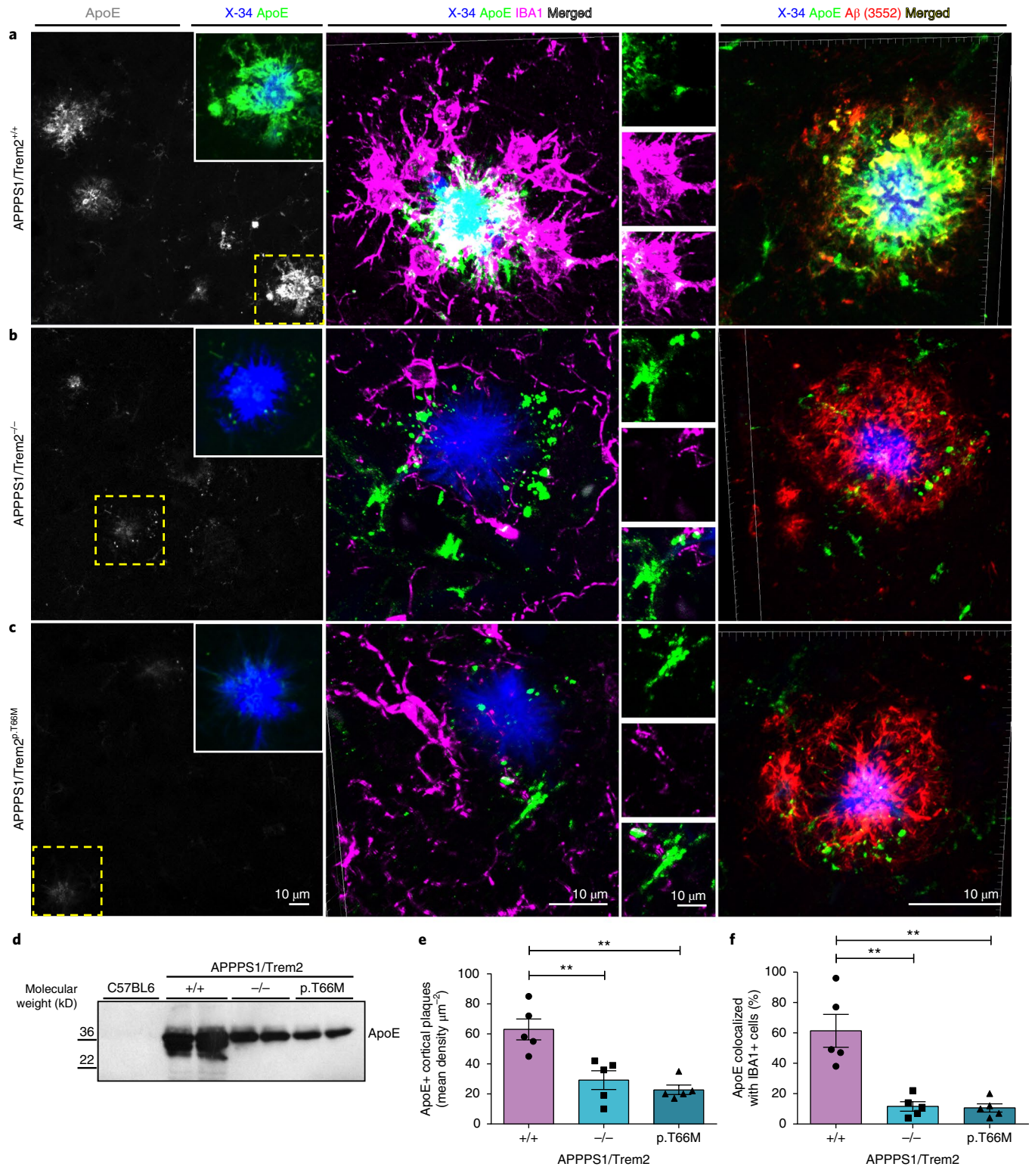

Reduced ApoE in amyloid plaques of AD patients with TREM2 variants. To test whether these preclinical findings have relevance for humans, we analyzed ApoE co-deposition in amyloid plaques in brains from AD patients with and without *TREM2* variants (Fig. 8 and Supplementary Fig. 5). Reduced ApoE colocalization with amyloid plaques was also observed in AD patients with the *TREM2* p.R47H, p.R62C, p.R62H, and p.D87N loss-of-function variants when compared with AD cases without *TREM2* variants (Fig. 8a–c and Supplementary Fig. 5a–c). ApoE reduction was most pronounced in cases with *TREM2* variants at amino acid 62, a position where an amino acid change has been confirmed to result in an increased risk for developing late-onset AD[33]. Reduced ApoE in amyloid plaques was further confirmed by western blotting of plaque-enriched formic acid extracts from brains with *TREM2* variants compared with those without *TREM2* coding variants, which was significant on normalization to $A\beta_{42}$ concentration (Fig. 8e,f and Supplementary Fig. 5f). Based on the findings in mouse brains (Fig. 2a,b and Supplementary Fig. 2), we expected that microglia in brains of *TREM2* mutation carriers should have a reduced capacity to cluster around amyloid plaques. Indeed large clusters of microglia around amyloid plaques were frequently found in AD cases without *TREM2* variants but were far less frequently detected in AD patients with *TREM2* loss-of-function variants (Fig. 8d,g and Supplementary Fig. 5d,g). While there was a trend in increased plaque-associated $A\beta_{42}$ with the number of E4 isoforms present, an ApoE genotype specific effect was not observed on plaque-associated microglia (Supplementary Fig. 5h,i). These data demonstrate that several independent *TREM2* coding variants all cause a loss of function of TREM2 resulting in reduced microglial clustering and ApoE accumulation in amyloid plaques.

Discussion

Our findings indicate that TREM2-dependent microglial functions limit amyloid plaque growth early but not late during the disease. For lowering amyloidogenesis, a TREM2-dependent activity is required that allows clustering of microglia around newly seeded amyloid plaques. In the presence of functional Trem2, phagocytic CD68-positive microglia accumulate around amyloid plaques and may initially promote Aβ clearance. Meanwhile, microglia that cluster around amyloid plaques increase ApoE expression[12,13,30] and may generate a microenvironment, which could lead to an increased ApoE concentration in the immediate neighborhood of Aβ deposits (Supplementary Fig. 6). In line with the well-described function of ApoE in amyloidogenesis[15–17], this may further promote Aβ aggregation and deposition. Consequently, high levels of ApoE in amyloid plaques may support their fibrillization and compaction, which is reflected by the longitudinal amyloid μPET imaging data. This is further supported by the recent finding that ApoE-deficient mice as well as mice expressing the AD-associated p.R47H TREM2 variant exhibit a striking reduction of plaque compaction[34,35]. In the absence of functional Trem2, microglia activation is dramatically reduced as shown by longitudinal TSPO μPET imaging. While using TSPO radiotracers to study neuroinflammation may present certain limitations, such as the presence of non-binders and unspecific binding to multiple types of immune cells including astrocytes[36], the high affinity for TSPO with better brain uptake, retention, clearance, and improved signal-to-noise ratio makes the enantiomerically stable tricyclic compound [^{18}F]-GE180 a suitable agent for imaging neuroinflammation in vivo[37–39]. Furthermore, the specificity of microglial activation has also been confirmed by in vitro autoradiography and immunohistochemistry using different transgenic models with varying degrees of neuroinflammation[10,28,40,41]. Nonetheless, future development of radioligands should facilitate in vivo detection of even more specific phenotypes of microglia activation.

Microglia clustering is abolished in Trem2 loss-of-function mice leading to reduced phagocytic amyloid plaque clearance but also to significantly less ApoE accumulation in amyloid plaques (both, in seeded and non-experimentally seeded cortical Aβ plaques; Supplementary Fig. 6). Reduced ApoE accumulation is in line with the finding that microglia lacking functional Trem2 suppress the disease-associated mRNA signature and appear to be locked in a homeostatic state with repressed ApoE expression[8,12–14,30]. Thus, absence of ApoE-expressing microglia in the immediate neighborhood of amyloid plaques may result in reduced ApoE co-aggregation in amyloid plaques (Supplementary Fig. 6), which is further supported by our finding that microglia depletion leads to a rather dramatic decline of plaque-associated ApoE. This also demonstrates that Trem2-dependent microglial uptake of ApoE[42] could not be the sole reason for increased ApoE in microglia, since on microglia depletion amyloid plaques should then contain higher and not lower ApoE levels. Thus, microglia may be one source of plaque-associated ApoE although an additional contribution of astrocytes cannot be excluded. For example, microglia may signal to astrocytes in a TREM2-dependent manner and may thus influence astroglial release of ApoE. Furthermore, the ApoE antibodies used may preferentially recognize a microglial ApoE variant. Future studies using ApoE antibodies that selectively recognize lipidated versus unlipidated ApoE could provide additional insights into potential mechanisms underlying our observations.

ApoE is predominantly synthesized in and secreted by astrocytes in non-diseased mouse[43] and human brain[44]. However, our study demonstrates that ApoE protein levels are strongly induced in plaque-associated microglia under disease conditions in a Trem2-dependent manner. This is in contrast to Trem2 loss-of-function microglia that are locked in a homeostatic state[8,14]. A limitation of our study is the use of murine *Trem2* and *Apoe* for investigating the interaction between microglia and amyloid pathology. Future studies should include humanized *TREM2* and *APOE* variants as these may influence Aβ metabolism and therefore amyloid pathogenesis[45]. With these limitations in mind, we studied the effect of *TREM2* coding variants in the AD patients. The observed reductions in plaque-associated microglia and ApoE in AD cases with *TREM2*

Fig. 7 | Decreased ApoE in cortical Aβ plaques after microglia depletion. a, Schematic outlining study design and timeline of GCV intracerebroventricular (icv) application and subsequent repopulation phase. **b**, An overview of fibrillar and immunopositive amyloid plaques co-stained with ApoE. Left: APPPS1/TK$^-$ mice show strong colocalization of amyloid plaques and ApoE compared with APPPS1/TK$^+$ mice (right). Right: Reduced plaque-associated ApoE shown at larger magnification. **c**, IMARIS 3D reconstructed high-resolution confocal images of co-stainings shown in **b**. White box indicates the area that is magnified for each immunostaining and placed adjacently. **d**,**e**, 3D reconstructed images of X-34/IBA1/ApoE/GFAP quadruple immunostaining in APPPS1/TK$^-$ and APPPS1/TK$^+$ mice. Channels from the same confocal image were split to focus on co-staining with IBA1 or GFAP individually. **d**, Left: X-34/ApoE/IBA1 co-staining shows increased IBA1 and ApoE colocalization with amyloid plaques in APPPS1/TK$^-$ mice compared with APPPS1/TK$^+$ mice (right). Smaller images placed adjacently display each channel separately and merged channels (indicated by white box). **e**, X-34/ApoE/GFAP immunostaining demonstrates no qualitative differences in APPPS1/TK$^-$ mice (left) compared with APPPS1/TK$^+$ mice (right). White box indicates the area that is magnified for each immunostaining and placed adjacently. **f**, Plaque-associated ApoE staining quantified from immunostainings shown in **b** and **c** ($n = 3$ mice/genotype, $P = 0.0034$). **g**, Quantification of percentage IBA1/ApoE ($n = 3$ mice per genotype, $P = 0.0004$) and GFAP/ApoE colocalization ($n = 3$ mice/genotype, $P = 0.4464$) from stainings displayed in **d** and **e**, respectively. Data represent mean ± s.d. Two-tailed unpaired *t* test with Welch's correction; NS, $P > 0.05$; $^{**}P < 0.005$; $^{***}P < 0.001$.

coding variants further support our findings and raise the possibility that microglial ApoE is induced in a TREM2-dependent manner in humans as well. To finally address this question, it will be important to study human microglial cells by single-cell sequencing.

Although we cannot fully exclude a saturation of amyloid plaque pathology late during disease progression in the *Trem2* loss-of-function mutants, it is tempting to speculate that early reduced plaque clearance in the absence of functional Trem2 may be opposed by less ApoE-driven amyloidogenesis later during disease progression. This could explain why late in the disease, levels of amyloid deposition converge in the presence and absence of functional Trem2. The age-dependent change in biphasic rate of amyloidogenesis observed in the absence of functional Trem2 is also consistent with the disease progression-dependent effects of Trem2 deficiency on

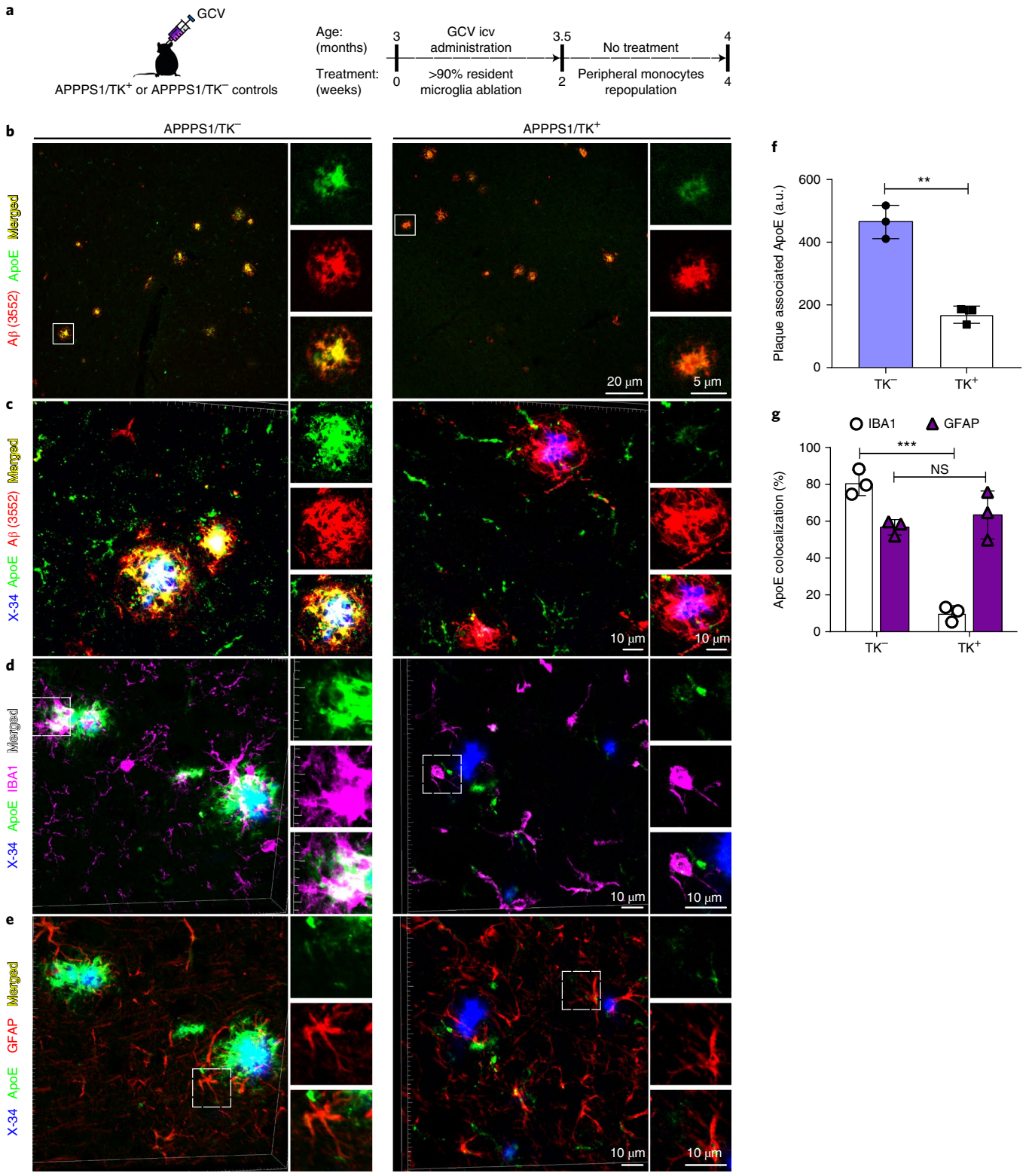

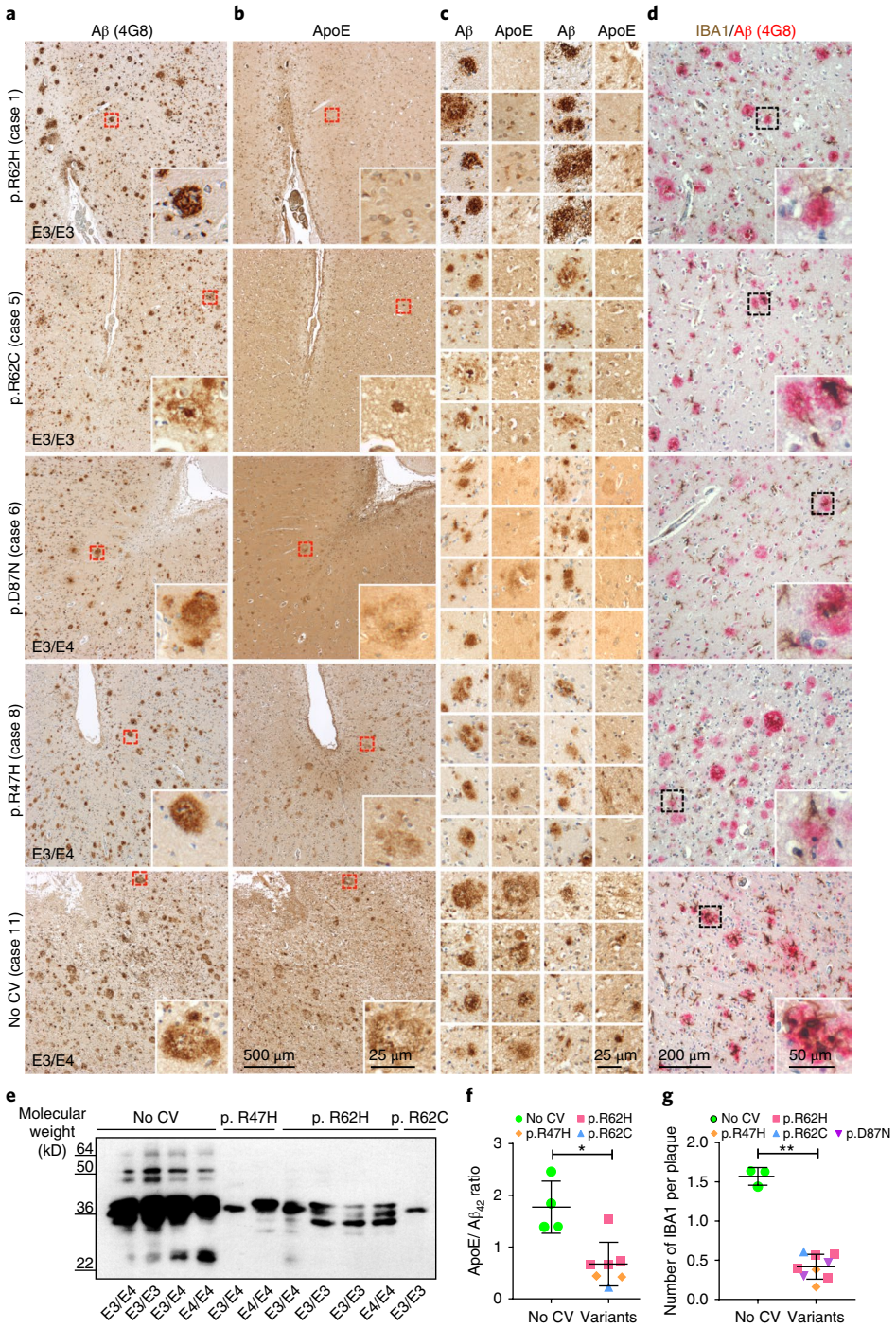

Fig. 8 | Reduced ApoE levels in Aβ plaques and impaired microglial clustering in *TREM2* coding variants. a, Temporal neocortex of human AD patients with and without the indicated *TREM2* variants stained for Aβ by 4G8 immunohistochemistry. **b**, In sections consecutive to those of the left column, AD patients with *TREM2* variants show reduced ApoE immunoreactivity within amyloid plaques compared with an AD case with no *TREM2* coding variants (no CV). Note that the ApoE reduction is most pronounced in cases with an amino acid exchange at position 62. Red boxes indicate the area in each staining that is magnified as inset. **c**, More examples of ApoE stainings comparing the same region in consecutive Aβ stained sections. **d**, IBA1 (brown) and 4G8 (red) co-staining in temporal neocortex. Microglia cells association with amyloid plaques as seen in a no-CV case (last row) is severely impaired in AD cases with different *TREM2* coding variants (rows 1–4). Furthermore, the overall density of microglial cells is reduced in *TREM2* variant AD cases when compared with no CV. Dotted black boxes indicate the area magnified as inset. **e**, ApoE immunoblotted in plaque-enriched formic acid fractions from cases shown in **a**–**d** and additional cases shown in Supplementary Fig. 5. Full image of the immunoblot is shown in Supplementary Fig. 7. **f**, ApoE/$A\beta_{42}$ ratio quantified from plaque-enriched formic acid fraction shows significantly decreased ApoE levels in AD cases with *TREM2* coding variants ($n^{R47H}=2$ cases, $n^{R62H}=4$ cases; $n^{R62C}=1$ case) compared with no CV ($n=4$ cases; $P=0.0121$). Of note, frozen material from p.D87N cases was not available and therefore not included. One of the no-CV cases was excluded due to diagnosed hepatitis. **g**, Number of IBA1-positive microglia per plaque quantified from images shown in **d** and Supplementary Fig. 5d ($n^{R47H}=2$ cases, $n^{R62H}=4$ cases; $n^{R62C}=1$ case; $n^{D87N}=2$ cases; $n^{no\ CV}=3$ cases; $P=3.9\times10^{-4}$). Noteworthy, sections from only three no CV cases were available in comparison to frozen material. No subjects were excluded in this analysis. Medial temporal cortex at the level of anterior hippocampus was used for all experiments. Data represent as mean ± s.d. Unpaired two-tailed *t* test with Welch's correction; $^{*}P<0.05$; $^{***}P<0.001$.

amyloid plaque deposition at late time points reported by Jay et al.[19]. However, at very early time points we observe differences in baseline levels of fibrillar amyloid pathology, which could be explained by slightly different ages, the use of different technologies, as well as regions of interest used to follow amyloidogenesis. In this regard, it needs to be considered that ^{18}F-florbetaben has a strong affinity to dense fibrillar amyloid plaques compared with diffuse amyloid deposition.

TREM2-dependent effects on ApoE load of amyloid plaques must be considered for any attempt to therapeutically modulate TREM2 and microglial function in general. Since we observe enhanced amyloidogenesis of *TREM2* mutants only at early stages of the disease, and since these differences may be compensated later by the reduced microglial production of ApoE, our findings support the observation that the disease is manifested decades before clinical symptoms occur[46]. AD-associated *TREM2* loss-of-function variants may thus promote seeding selectively at an early phase of the disease. Seeded plaques have been reported to be neurotoxic by decreasing neurogenesis and increasing neuronal cell death in their immediate neighborhood[47]. Thus by eliminating newly seeded plaques, TREM2 may have protective functions at least early during amyloidogenesis. A protective function of TREM2 is also supported by the finding that disease-associated *TREM2* variants cause a loss of function (for example, refs. [10,11,42,48]). This is consistent with the finding of increased soluble TREM2 in cerebrospinal fluids of patients of the Dominantly Inherited Alzheimer Network (DIAN) cohort already five years before onset of clinical symptoms, which may reflect a defensive microglial activation at an early state of the disease[49]. However, microglia not only modulate amyloid plaque clearance but also provide ApoE as an Aβ aggregation factor[17], which could consequently facilitate amyloidogenesis. Finally, our finding that microglia influence amyloid plaque fibrillarity depending on their activation state is highly relevant for clinical studies as longitudinal amyloid PET is a read-out for amyloid-based therapies[50].

Online content

Any methods, additional references, Nature Research reporting summaries, source data, statements of data availability and associated accession codes are available at https://doi.org/10.1038/s41593-018-0296-9.

Received: 19 January 2018; Accepted: 14 November 2018;
Published online: 7 January 2019

References

1. Jucker, M. & Walker, L. C. Self-propagation of pathogenic protein aggregates in neurodegenerative diseases. *Nature* **501**, 45–51 (2013).
2. Meyer-Luehmann, M. et al. Exogenous induction of cerebral beta-amyloidogenesis is governed by agent and host. *Science* **313**, 1781–1784 (2006).
3. Butovsky, O. & Weiner, H. L. Microglial signatures and their role in health and disease. *Nat. Rev. Neurosci.* **19**, 622–635 (2018).
4. Song, W. M. & Colonna, M. The identity and function of microglia in neurodegeneration. *Nat. Immunol.* **19**, 1048–1058 (2018).
5. Ulrich, J. D., Ulland, T. K., Colonna, M. & Holtzman, D. M. Elucidating the role of *TREM2* in Alzheimer's disease. *Neuron* **94**, 237–248 (2017).
6. Guerreiro, R. et al. *TREM2* variants in Alzheimer's disease. *N. Engl. J. Med.* **368**, 117–127 (2013).
7. Jonsson, T. et al. Variant of *TREM2* associated with the risk of Alzheimer's disease. *N. Engl. J. Med.* **368**, 107–116 (2013).
8. Mazaheri, F. et al. *TREM2* deficiency impairs chemotaxis and microglial responses to neuronal injury. *EMBO Rep.* **18**, 1186–1198 (2017).
9. Ulland, T. K. et al. *TREM2* maintains microglial metabolic fitness in Alzheimer's disease. *Cell* **170**, 649–663.e13 (2017).
10. Kleinberger, G. et al. The FTD-like syndrome causing *TREM2* T66M mutation impairs microglia function, brain perfusion, and glucose metabolism. *EMBO J.* **36**, 1837–1853 (2017).
11. Kleinberger, G. et al. *TREM2* mutations implicated in neurodegeneration impair cell surface transport and phagocytosis. *Sci. Transl. Med.* **6**, 243ra86 (2014).
12. Butovsky, O. et al. Identification of a unique TGF-β-dependent molecular and functional signature in microglia. *Nat. Neurosci.* **17**, 131–143 (2014).
13. Keren-Shaul, H. et al. A unique microglia type associated with restricting development of Alzheimer's disease. *Cell* **169**, 1276–1290.e17 (2017).
14. Krasemann, S. et al. The TREM2-APOE pathway drives the transcriptional phenotype of dysfunctional microglia in neurodegenerative diseases. *Immunity* **47**, 566–581.e9 (2017).
15. Liu, C. C. et al. ApoE4 accelerates early seeding of amyloid pathology. *Neuron* **96**, 1024–1032.e3 (2017).
16. Huynh, T. V. et al. Age-dependent effects of apoE reduction using antisense oligonucleotides in a model of β-amyloidosis. *Neuron* **96**, 1013–1023.e4 (2017).
17. Ma, J., Yee, A., Brewer, H. B. Jr, Das, S. & Potter, H. Amyloid-associated proteins α1-antichymotrypsin and apolipoprotein E promote assembly of Alzheimer β-protein into filaments. *Nature* **372**, 92–94 (1994).
18. Liao, F. et al. Targeting of nonlipidated, aggregated apoE with antibodies inhibits amyloid accumulation. *J. Clin. Invest.* **128**, 2144–2155 (2018).
19. Jay, T. R. et al. Disease progression-dependent effects of TREM2 deficiency in a mouse model of Alzheimer's disease. *J. Neurosci.* **37**, 637–647 (2017).
20. Wang, Y. et al. TREM2-mediated early microglial response limits diffusion and toxicity of amyloid plaques. *J. Exp. Med.* **213**, 667–675 (2016).
21. Jay, T. R. et al. TREM2 deficiency eliminates TREM2+inflammatory macrophages and ameliorates pathology in Alzheimer's disease mouse models. *J. Exp. Med.* **212**, 287–295 (2015).
22. Wang, Y. et al. TREM2 lipid sensing sustains the microglial response in an Alzheimer's disease model. *Cell* **160**, 1061–1071 (2015).
23. Kane, M. D. et al. Evidence for seeding of β-amyloid by intracerebral infusion of Alzheimer brain extracts in β-amyloid precursor protein-transgenic mice. *J. Neurosci.* **20**, 3606–3611 (2000).
24. Radde, R. et al. Abeta42-driven cerebral amyloidosis in transgenic mice reveals early and robust pathology. *EMBO Rep.* **7**, 940–946 (2006).
25. Turnbull, I. R. et al. Cutting edge: TREM-2 attenuates macrophage activation. *J. Immunol.* **177**, 3520–3524 (2006).
26. Guerreiro, R. J. et al. Using exome sequencing to reveal mutations in TREM2 presenting as a frontotemporal dementia-like syndrome without bone involvement. *JAMA Neurol.* **70**, 78–84 (2013).
27. Ulrich, J. D. et al. Altered microglial response to Aβ plaques in APPPS1-21 mice heterozygous for TREM2. *Mol. Neurodegener.* **9**, 20 (2014).
28. Brendel, M. et al. Increase of TREM2 during aging of an Alzheimer's disease mouse model is paralleled by microglial activation and amyloidosis. *Front. Aging Neurosci.* **9**, 8 (2017).
29. Dickens, A. M. et al. Detection of microglial activation in an acute model of neuroinflammation using PET and radiotracers 11C-(R)-PK11195 and 18F-GE-180. *J. Nucl. Med.* **55**, 466–472 (2014).
30. Holtman, I. R. et al. Induction of a common microglia gene expression signature by aging and neurodegenerative conditions: a co-expression meta-analysis. *Acta Neuropathol. Commun.* **3**, 31 (2015).
31. Grathwohl, S. A. et al. Formation and maintenance of Alzheimer's disease β-amyloid plaques in the absence of microglia. *Nat. Neurosci.* **12**, 1361–1363 (2009).
32. Heppner, F. L. et al. Experimental autoimmune encephalomyelitis repressed by microglial paralysis. *Nat. Med.* **11**, 146–152 (2005).
33. Sims, R. et al. Rare coding variants in *PLCG2*, *ABI3*, and *TREM2* implicate microglial-mediated innate immunity in Alzheimer's disease. *Nat. Genet.* **49**, 1373–1384 (2017).
34. Ulrich, J. D. et al. ApoE facilitates the microglial response to amyloid plaque pathology. *J. Exp. Med.* **215**, 1047–1058 (2018).
35. Cheng-Hathaway, P. J. et al. The Trem2 R47H variant confers loss-of-function-like phenotypes in Alzheimer's disease. *Mol. Neurodegener.* **13**, 29 (2018).
36. Lavisse, S. et al. Reactive astrocytes overexpress TSPO and are detected by TSPO positron emission tomography imaging. *J. Neurosci.* **32**, 10809–10818 (2012).
37. Chau, W. F. et al. Exploration of the impact of stereochemistry on the identification of the novel translocator protein PET imaging agent [^{18}F] GE-180. *Nucl. Med. Biol.* **42**, 711–719 (2015).
38. Feeney, C. et al. Kinetic analysis of the translocator protein positron emission tomography ligand [^{18}F]GE-180 in the human brain. *Eur. J. Nucl. Med. Mol. Imaging* **43**, 2201–2210 (2016).
39. Vomacka, L. et al. TSPO imaging using the novel PET ligand [^{18}F]GE-180: quantification approaches in patients with multiple sclerosis. *EJNMMI Res.* **7**, 89 (2017).
40. Boutin, H. et al. 18F-GE-180: a novel TSPO radiotracer compared to 11C-R-PK11195 in a preclinical model of stroke. *Eur. J. Nucl. Med. Mol. Imaging* **42**, 503–511 (2015).
41. James, M. L. et al. [^{18}F]GE-180 PET detects reduced microglia activation after LM11A-31 therapy in a mouse model of Alzheimer's disease. *Theranostics* **7**, 1422–1436 (2017).
42. Yeh, F. L., Wang, Y., Tom, I., Gonzalez, L. C. & Sheng, M. TREM2 binds to apolipoproteins, including APOE and CLU/APOJ, and thereby facilitates uptake of amyloid-beta by microglia. *Neuron* **91**, 328–340 (2016).

43. Zhang, Y. et al. An RNA-sequencing transcriptome and splicing database of glia, neurons, and vascular cells of the cerebral cortex. *J. Neurosci.* **34**, 11929–11947 (2014).
44. Zhang, Y. et al. Purification and characterization of progenitor and mature human astrocytes reveals transcriptional and functional differences with mouse. *Neuron* **89**, 37–53 (2016).
45. Fagan, A. M. et al. Human and murine ApoE markedly alters Aβ metabolism before and after plaque formation in a mouse model of Alzheimer's disease. *Neurobiol. Dis.* **9**, 305–318 (2002).
46. Sperling, R., Mormino, E. & Johnson, K. The evolution of preclinical Alzheimer's disease: implications for prevention trials. *Neuron* **84**, 608–622 (2014).
47. Ziegler-Waldkirch, S. et al. Seed-induced Aβ deposition is modulated by microglia under environmental enrichment in a mouse model of Alzheimer's disease. *EMBO J.* **37**, 167–182 (2018).
48. Song, W. M. et al. Humanized TREM2 mice reveal microglia-intrinsic and -extrinsic effects of R47H polymorphism. *J. Exp. Med.* **215**, 745–760 (2018).
49. Suárez-Calvet, M. et al. Early changes in CSF sTREM2 in dominantly inherited Alzheimer's disease occur after amyloid deposition and neuronal injury. *Sci. Transl. Med.* **8**, 369ra178 (2016).
50. Sevigny, J. et al. The antibody aducanumab reduces Aβ plaques in Alzheimer's disease. *Nature* **537**, 50–56 (2016).

Acknowledgements

This work was supported by the Deutsche Forschungsgemeinschaft (DFG) within the framework of the Munich Cluster for Systems Neurology (EXC 1010 SyNergy), a DFG funded Koselleck Project (HA1737/16-1 to C.H.), by the Helmholtz-Gemeinschaft Zukunftsthema 'Immunology and Inflammation' (ZT-0027 to C.H.), the FOR2290 (to S.F.L. and C.H.), and by a dedicated PET imaging grant to M.B. and A.R. (BR4580/1-1 & RO5194/1-1). This project has received additional funding from the Innovative Medicines Initiative 2 Joint Undertaking under grant agreement No. 115976. Startup funding for this project came from LMU^{excellent}. Additional funding came from the general legacy of S. Ammer, the MetLife award, and the Cure Alzheimer's fund. M.M.-L. is supported by the Emmy Noether Program of the DFG (ME 3542/1-1). M.M.-L. and S.F.L. are supported by the Hans and Ilse Breuer Foundation. S.T. got support from Ono Pharmaceuticals, Japan. D.M.H. is supported by NIH grants NS090934 and AG047644, the JPB Foundation, and the Cure Alzheimer's Fund. S.F.L. is supported by the Centers of Excellence in neurodegeneration and the Helmholtz-Israel program. O.B. is supported by NIH grants NINDS (R01NS088137), NIH-NIA (R01AG051812), NIH-NIA (R01AG054672) and the Cure Alzheimer's Fund. The APPPS1 colony was established from a breeding pair kindly provided by M. Jucker (Hertie-Institute for Clinical Brain Research, University of Tübingen and DZNE-Tübingen). The authors thank M. Colonna for the Trem2$^{-/-}$ mice. Thanks to the Queen Square Brain Bank for access to tissue: this resource is funded in part by the Weston Foundation and the MRC. D.E. is supported by the European Community's Health Seventh Framework Programme under grant agreement 617198 [DPR-MODELS].

Author contributions

C.H., M.M.-L., G.K., and S.P. conceived the study and analyzed the results. C.H. wrote the manuscript with help from M.M.-L., S.P., T.A., G.K., M.B., and D.M.H. and further input from all co-authors. S.P. and N.K. performed seeding experiments; S.P. and M.X. performed the ApoE stainings. B.N. performed Aβ ELISA. M.B., M.D., C.F., P.B., and A.R. performed PET imaging and quantitative PET analyses. G.E. made GE180 cassettes available through an early access model. A.E., A.G. and S.P. performed the three-dimensional image analyses. O.B. and S.K. provided independent immunohistochemical data and interpretation on ApoE. D.M.H. interpreted the ApoE stainings and provided appropriate ApoE antibodies. T.A. and J.H. provided human brain sections and interpreted the immunohistochemical analyses. G.K. and N.P. performed *TREM2* sequencing and D.E. performed *PSEN1*, *PSEN2* and *APP* sequencing of human autopsy cases. S.T., A.C., L.S.M., S.A.M., and S.F.L. prepared primary microglial lysates and measured ApoE levels by mass spectrometry. M.W. provided technical advice for protein extraction and ApoE experiments. S.A.G. and J.J.N. provided brain sections from microglia-depleted mice.

Competing interests

C.H. collaborates with Denali and received a speaker honorarium of Roche and Novartis. D.M.H. co-founded and is on the scientific advisory board of C2N Diagnostics. D.M.H. consults for Denali, Eli Lilly, Glaxosmithkline, and AbbVie. A.R. received consultant and speaker honoria from Piramal Imaging and GE Healthcare. O.B. collaborates with Sanofi. S.T. collaborates with Ono Pharmaceuticals (Japan). S.A.G is an employee of Neurimmune AG. All other authors declare no competing interests.

Additional information

Supplementary information is available for this paper at https://doi.org/10.1038/s41593-018-0296-9.

Reprints and permissions information is available at www.nature.com/reprints.

Correspondence and requests for materials should be addressed to M.M. or C.H.

Publisher's note: Springer Nature remains neutral with regard to jurisdictional claims in published maps and institutional affiliations.

Methods

Transgenic mice. All animal experiments were approved by the Bavarian government and performed in accordance with local animal handling laws. Four-month-old male APPPS1 transgenic mice (Thy1-APP$^{695KM670/671NL}$; Thy-1PS1^{L166P})[24] and age-matched male C57BL6 littermate controls were used. Using male mice ensured reduced gender-dependent variability in plaque deposition[24].

APPPS1 mice were crossed to Trem2$^{-/-}$ mice[25] and maintained on a C57BL6J background. Additionally, APPPS1 were crossed to achieve homozygous Trem2 p.T66M knock-in mice[10], which were maintained on a mixed genetic background (N1 backcross to C57BL6N). The Trem2 p.T66M mice were compared with APPPS1/Trem2$^{+/+}$ mice from the same background for all experiments. No differences were observed between wild-type control mice from the Trem2$^{-/-}$ or Trem2 p.T66M mouse lines. For µPET experiments, 3-, 6-, and 12-month-old female APPPS1/Trem2$^{+/+}$ and age-matched APPPS1/Trem2$^{-/-}$ were used. As additional controls, non-transgenic age-matched female C57BL7/Trem2$^{+/+}$ as well as C57BL6/Trem2$^{-/-}$ were included.

Randomization and blinding. For all animal experiments, mice were allocated randomly after genotyping. Mice of different genotype were allocated randomly to PET experiments with scan number and slot, as well as with blinded identity to the experimenter using a chipping system. Investigator was not blinded during the intrahippocampal injection experiments. All the immunohistochemical analysis was initially performed blinded; however, due the strong microglial-clustering impairment phenotype of mice with loss of Trem2 function, complete blinding was not possible. Slides were imaged and saved with random numbers to identify them. Images were then quantified and unblinded to perform group statistics. No statistical methods were used to pre-determine sample sizes but our sample sizes were based on previous findings[2,10,28,31].

Preparation of brain homogenate for intracerebral injections. Brain homogenates for injection were prepared as previously described[2]. Mouse brain extracts were prepared by dissecting the neocortex of 15-month-old female APPPS1 transgenic mice and age-matched non-transgenic C57BL6 controls. Tissue samples were homogenized at 10% (w/v) in sterile PBS, vortexed, sonicated 3×5 s (Bandelin Sonorex RK100H), and centrifuged at 3,000×*g* for 5 min at 4 °C. The supernatant was aliquoted and frozen at −80 °C until use.

Stereotaxic surgery. Six-week-old asymptomatic host mice were anesthetized with a mixture of medetomidin (0.05 mg^{-1} kg^{-1}), midazolam (5 mg^{-1} kg^{-1}), and fentanyl (0.5 mg^{-1} kg^{-1}). As previously described[2], a 0.5–1.0-cm-long incision was made in the shaved and sterilized skin to expose the bregma. Bilateral stereotaxic injections of mouse brain homogenate (1.25 µl min^{-1} over 2 min) were performed with a Hamilton syringe into the hippocampi and overlaying cortices at specific stereotaxic coordinates (anterior–posterior −2.3 mm, medial–lateral +/−2.0 mm, dorsal–ventral −0.8/−2.0 mm). The needle was retained for additional 2 min before it was slowly withdrawn. The incision was cleaned with povidone-iodine antiseptic solution and sutured. Following this, mice were brought out of anesthesia using a mixture of atipamezol (2.5 mg^{-1} kg^{-1}), flumazenil (0.5 mg^{-1} kg^{-1}), and naloxone (1.2 mg^{-1} kg^{-1}), returned to clean cages, and monitored until recovery from anesthesia. Mice were weighed and monitored daily for seven days following surgery. Food and water was provided ad libitum.

Immunofluorescence analyses of mouse brains. Brains were removed after transcardial perfusion with PBS and dissected into two hemispheres. The left hemibrain was immersion-fixed for 48 h in 4% paraformaldehyde, followed by cryoprotection in 30% sucrose for 48 h. After freezing, 25 µm microtome sections were sequentially collected in PBS with 15% glycerol and kept at −80 °C until further use. For staining, heat-induced sodium citrate antigen retrieval was performed using 25 mM sodium citrate with 0.05% Tween-20 at 95 °C for 30 min. Free-floating sections were incubated in X-34 for 1 h at room temperature in 60% PBS/40% EtOH mix; pH was adjusted with 1 N NaOH[51]. Sections were washed briefly with 60% PBS/40% EtOH before blocking. Primary antibodies (Supplementary Table 1) were added and the sections were kept at 4 °C overnight with slow agitation. For Trem2 staining, sections were incubated at 4 °C for two nights. After applying the appropriate secondary antibodies, tissue sections were stained with ThioS (0.01%) or 4′,6-diamidin-2-phenylindol (DAPI, 5 µg ml^{-1}) before mounting sections onto slides (Prolong Gold Antifade reagent, Thermo Fisher Scientific).

Confocal imaging and analyses. Images were acquired using a LSM 710 Confocal microscope (Zeiss) and the ZEN 2011 software package (black edition, Zeiss). Laser and detector settings were maintained constant for the acquisition of each immunostaining. For all analyses, at least three images were taken per brain region and slide using ×20 objective and ×63 oil differential interference contrast objective, respectively, at 2,048×2,048 pixel resolution, with *z*-step size of 2 µm at 16 µm thickness. High-resolution stacks imaged by confocal microscopy were 3D reconstructed using IMARIS 8 software.

For quantification of plaque densities, acquired images were imported to Fiji software (ImageJ) and data channels were separated (image/color/split channels). Gaussian filtering was used to remove noise and intensity distribution for each image was equalized using a rolling ball algorithm, which is implemented as background subtraction plugin in Fiji. For the feasibility of the quantification, all layers from a single image stack were projected on a single slice (stack/Z projection). Next, the plaques were segmented using automatic thresholding methods in Fiji (with 'Moments' thresholding setting for microglial stainings and 'Otsu' for plaques and ApoE). Subsequently, the dentate gyrus was selected manually whereupon the area as well as the cumulative area of the segmented plaques were calculated in the region of interest. Finally, the coverage of segmented plaques over the area of dentate gyrus was calculated, indicating the distribution of segmented plaques in the dentate gyrus. Similar thresholding was used to quantify cortical plaques as well as IBA1, CD68, and ApoE stainings. The number of IBA1 and CD68-positive microglia around plaques were counted in the cortex over the length of layers 3–5 using ImageJ.

In vivo µPET imaging and quantification. All µPET procedures followed an established standardized protocol for radiochemistry, acquisition, and post-processing[52,53]. In brief, ^{18}F-GE180 TSPO µPET with an emission window of 60–90 min post injection was used to measure cerebral microglial activity, and ^{18}F-florbetaben amyloid µPET with an emission window of 30–60 min post injection was used for assessment of fibrillar cerebral amyloidogenesis. APPPS1/Trem2$^{-/-}$ and age-matched APPPS1/Trem2$^{+/+}$ mice were longitudinally studied from 6 to 12 months of age using dual µPET. All analyses were performed by PMOD (V3.4, PMOD Technologies). Normalization of injected activity was performed by the previously validated myocardium correction method[54] for TSPO µPET and by a white matter reference region for amyloid µPET.

TSPO and amyloid µPET estimates (absolute values and percentage changes over time) deriving from the same large neocortical target volume of interest (50 mm^3) were extracted and compared between the two age and genotype groups by a Student's *t*-test. In-house scans of C57BL6 mice served for generation of *Z*-score deviation images for both tracers (Z-score = (average$_{APPPS1/TREM2^{-/-}}$ − average$_{C57BL6}$)/SD$_{C57BL6}$) or (average$_{APPPS1/TREM2^{+/+}}$ − average$_{C57BL6}$)/SD$_{C57BL6}$). Percentage changes with baseline as starting point were calculated such that the earliest time interval was set as 3–4 months and the latest at 11–12, depicted as 3 and 11 months.

Patient material. Tissue samples of patient autopsy cases were provided by the Neurobiobank Munich, Ludwig-Maximilians-University (LMU) Munich, and Queen Square Brain Bank for Neurological Disorders, University College London (UCL). Detailed clinical characteristics were ascertained from an integrated autopsy database at respective brain banks. Written informed consent for autopsy and analysis of tissue sample data was obtained for all patients, either from the patients themselves or their next of kin. All samples were collected according to the guidelines of the local ethics committee following all ethical regulations. All requirements for written informed consent was waived by the medical ethics committee that approved the study protocol. Information on cases regarding brain bank, clinical diagnosis age at death, post-mortem delay, AD Braak and Braak stage, *TREM2* coding variant, and *APOE* status is given in Supplementary Table 2. Sample sizes were based on availability of patient material. For all experiments, temporal neocortex was used which included cortex of medial temporal gyrus at the level of anterior hippocampus.

Genotyping of AD cases. To identify *TREM2* variant carriers within the Neurobiobank Munich *TREM2* exon 2 was amplified from genomic DNA by PCR, purified using ExoSAP-IT (Thermo Fisher Scientific) and sequenced by standard Sanger sequencing (GATC Biotech). Sequences were aligned to the *TREM2* reference sequence (UCSC Genome Browser, assembly GRCh38/hg38; chr6:41,158,506–41,163,186) and variants called manually by two investigators using the CLC Main Workbench Software (Qiagen). To identify pathogenic *APP*, *PSEN1*, and *PSEN2* mutations all cases were additionally sequenced using a TruSeq CustomAmplicon kit on a MiSeq (Illumina) according to the protocol from the manufacturer. Panel sequencing confirmed all *TREM2* variants and was also used to determine the *APOE* genotype.

Immunohistochemistry on human post-mortem brain tissue. Temporal neocortex sections of 5 µm thickness were cut from paraffin-embedded specimens. For immunohistochemistry, all slides were deparaffinized and rehydrated in a series of xylene and graded ethanol. The sections were subjected to citric acid antigen retrieval (1 M sodium citrate in PBS, pH 6.0) and boiled in a microwave for 20 min. After cooling, endogenous peroxidase activity was quenched using 30% hydrogen peroxide for 20 min. Sections were blocked and incubated with primary antibody (Supplementary Table 1) overnight at 4 °C. Primary antibodies were detected with biotinylated anti-mouse and anti-rabbit immunoglobulin-G secondary antibodies and visualized with avidin-biotin-complex (ABC-Kit, Vector Laboratories) followed by development with diaminobenzidine-HCl (DAB, Vector Laboratories) for 5 min. Lastly, sections were counterstained with haematoxylin. Stainings were performed in serially cut sections to compare the same region of interest through all immunostainings. For IBA1/4G8 co-stainings, mouse alkaline phosphatase (AP)-conjugated and rabbit horseradish peroxidase (HRP)-conjugated

secondary antibodies were incubated at room temperature for 1 h. HRP staining was developed using DAB as mentioned above and AP staining was developed using Permanent AP Red Kit for 20 min at room temperature (Zytomed Systems). We controlled for artifacts resulting from long formaldehyde fixation period by comparing different antigen retrieval methods as well as staining freshly fixed frozen tissue. Brightfield images were taken by CellD, Olympus BX50 Soft Imaging System (Olympus). Plaque-associated ApoE in human temporal neocortex was quantified using the 'Analyze Particles' feature in ImageJ. All thresholded ('Otsu') and masked plaques were selected from the regions of interest manager, and used to measure ApoE in the ApoE-stained serial section. Images from similar regions of interest were taken in all samples, including the superior, middle, and inferior temporal gyri using ×4 as well as ×10 objectives for a better overview of the tissue. Amyloid plaques in the subcortical white matter were not analyzed. The number of IBA1-positive microglia per cortical plaque was scored and counted from 6–10 images per slide. A total of 2,461 plaques were analyzed and only IBA1-positive microglia with visibly stained nuclei were counted.

Preparation of protein extracts from brain. After transcardial perfusion with PBS, the right hemibrain was further dissected on ice to isolate mouse hippocampi and cortices, which were frozen at −80 °C until use. Frozen mouse or human tissue was weighed and homogenized with 500 µl DEA buffer (50 mM NaCl, 0,2% diethylamine, pH 10, supplemented with 2X protease inhibitor (P8340, Sigma-Aldrich)) using the Precellys 24 homogenizer (Bertin Instruments) with the CKMix Tissue Homogenizing Kit (2 ml tubes, VWR) under vacuum for 30 s at 6,500 r.p.m. at 4 °C. This homogenate was centrifuged for 5 min at 4 °C at 5,000 × *g* to pellet DEA-insoluble material and the supernatant was ultracentrifuged for 1 h at 100,000 × *g* with a TLA55 rotor in an Optima MAX-XP ultracentrifuge (Beckman Coulter) to obtain the DEA extracts which were neutralized with 10% 1 M Tris pH 6.8. From the remaining cellular pellet, proteins were extracted with RIPA buffer (20 mM Tris-HCl, pH 7.5, 150 mM NaCl, 1 mM EDTA, 1% NP-40, 1% sodium deoxycholate, 2.5 mM sodium pyrophosphate plus protease inhibitor) using the Precellys 24 under vacuum for 10 s at 5,000 r.p.m. After a 5 min clearing for RIPA-insoluble material at 5,000 × *g* at 4 °C, the supernatant was again ultracentrifuged as above to obtain the RIPA-soluble protein fraction. The RIPA-insoluble pellet was dissolved with ice-cold 70% formic acid and sonicated for 7 min at room temperature using a Sonorex RK100H (Bandelin) followed by a final ultracentrifugation as above. The formic acid soluble fractions were supplemented and neutralized using 10 volumes of 1 M Tris pH 9.5 plus protease inhibitor. Protein concentrations were measured for DEA and RIPA fractions using a BCA assay (Pierce). All samples were aliquoted and frozen at −80 °C until use.

Aβ ELISA. Aβ was quantified by a sandwich immunoassay using the Meso Scale Discovery SECTOR Imager 2400 as described previously[55]. Samples were extracted in formic acid as described above and measured in duplicates.

Immunoblotting. For amyloid plaques and ApoE western blots, equal volumes of formic acid extracted sample were subjected to 10–20% Tris-tricine gels (1 mm, Novex) and 10% Tris-glycine gels, respectively, under denaturing conditions. After separation, proteins were transferred onto nitrocellulose membranes (Protran BA85; GE Healthcare), boiled in PBS for 5 min and blocked in I-Block solution (0.2% Tropix I-Block (Applied Biosystems), 0.1% Tween-20 in PBS) for 1 h at room temperature with agitation. To detect different brain cell types from microglia-enriched and microglia-depleted lysates, 1 µg of total protein was loaded on 12% Tris-glycine gels and run under denaturing conditions. Proteins were subsequently transferred onto polyvinylidene difluoride membranes (PVDF Immobilon-P; Merck Millipore) and blocked in I-Block solution for 1 h at room temperature. Primary antibodies (HJ6.3, Murine ApoE; 6E10, Aβ1–16; IBA1; GFAP; Tuj1; CNPase; HJ15.7, Human ApoE) were diluted in I-Block solution or TBS-Tween and incubated overnight at 4 °C with agitation. Blots were washed with TBS-Tween and incubated in corresponding HRP-conjugated secondary antibodies for 1 h at room temperature and visualized using enhanced chemiluminescence technique (Pierce).

Relative protein quantification of ApoE in microglia-enriched and -depleted fractions by mass spectrometry. Microglia isolation was performed using the magnetic activated cell sorting technology as described previously[56]. Microglia-enriched and -depleted samples were prepared from three APPPS1 as well as three wild-type mice each at the age of 3, 6, and 12 months. Additionally, microglia-enriched and -depleted fractions were prepared for 12-month-old APPPS1/Trem2$^{+/+}$ and age-matched APPPS1/Trem2$^{-/-}$ mice. Both fractions were lysed in lysis buffer (50 mM Tris, 150 mM NaCl, 2 mM EDTA, 1% Triton X-100, pH 7.5). A protein amount of 15 µg per sample was digested with LysC and trypsin using the filter-aided sample preparation protocol[57]. The resulting peptides were concentrated using self-made C18 stage tips[58]. The eluted peptides were concentrated by vacuum centrifugation and analyzed by nanoscale liquid chromatographic tandem mass spectrometry (nLC-MS/MS) using an Easy nLC 1000 coupled online via a Nanospray Flex ion source (both Thermo Fisher Scientific) equipped with a PRSO-V1 column oven (Sonation) to a Q Exactive high-field mass spectrometer (Thermo Fisher Scientific). Briefly, 1.3 µg of peptides were separated on a self-packed 30 cm column (Reprosil-Pur 120 C18-AQ, 1.9 µm, Dr Maisch) using a binary gradient of water (A) and acetonitrile (B) supplemented with 0.1% formic acid at 50 °C and a flow rate of 250 nl min^{-1} (0 min, 2% B; 3:30 min, 5% B; 137:30 min, 25% B; 168:30 min, 35% B; 182:30 min, 60% B; 185 min, 95% B; 200 min, 95% B).

A data-independent acquisition method using sequential window acquisition of all theoretical mass spectra from *m/z* 300–1,400 was applied (25 windows). Full MS spectra were acquired at a resolution of 120,000, whereas fragment-ion spectra were recorded at a resolution of 30,000. Data analysis and label-free protein quantification was performed with the software Spectronaut (version 11.0.15038.4.29119, Biognosys)[59] using a microglia spectral library. The library was generated with the software Maxquant (version 1.5.5.1)[60] using a top-15 data-dependent acquisition method on the basis of a reviewed canonical UniProt database of *Mus musculus* (download: 11 January 2017, 16,844 entries). The false discovery rate, for both peptides and proteins, was adjusted to less than 1%. Two unique peptides were required for protein quantification using standard settings. Here, only ApoE label-free quantification intensities were extracted and subjected to statistical analysis.

Statistical analysis. Data are presented as mean ± s.e.m unless otherwise stated. Data were checked for normality using the Shapiro–Wilk method, the D'Agostino and Pearson normality test, and the Kolmogorov–Smirnov normality test. Statistical significance was calculated by one-way analysis of variance (ANOVA) followed by Dunnett's post hoc test for group-wise comparisons unless otherwise stated. The label-free protein quantification intensities were $\log^2$-transformed and a Student's *t*-test was applied to calculate statistical significance. Amyloid and microglia stainings were correlated with amyloid and TSPO µPET, respectively, using Pearson correlation coefficients and linear regression analyses. A *P* value of less than 0.05 was considered significant.

Reporting Summary. Further information on research design is available in the Nature Research Reporting Summary linked to this article.

Data availability

The data that support the findings of this study are available from the corresponding author upon reasonable request.

References

51. Styren, S. D., Hamilton, R. L., Styren, G. C. & Klunk, W. E. X-34, a fluorescent derivative of Congo red: a novel histochemical stain for Alzheimer's disease pathology. *J. Histochem. Cytochem.* **48**, 1223–1232 (2000).
52. Brendel, M. et al. Glial activation and glucose metabolism in a transgenic amyloid mouse model: a triple-tracer PET study. *J. Nucl. Med.* **57**, 954–960 (2016).
53. Overhoff, F. et al. Automated spatial brain normalization and hindbrain white matter reference tissue give improved [^{18}F]-florbetaben PET quantitation in Alzheimer's model mice. *Front. Neurosci.* **10**, 45 (2016).
54. Deussing, M. et al. Coupling between physiological TSPO expression in brain and myocardium allows stabilization of late-phase cerebral [^{18}F]GE180 PET quantification. *Neuroimage* **165**, 83–91 (2018).
55. Page, R. M. et al. Generation of $A\beta_{38}$ and $A\beta_{42}$ is independently and differentially affected by familial Alzheimer disease-associated presenilin mutations and γ-secretase modulation. *J. Biol. Chem.* **283**, 677–683 (2008).
56. Daria, A. et al. Young microglia restore amyloid plaque clearance of aged microglia. *EMBO J.* **36**, 583–603 (2017).
57. Wiśniewski, J. R., Zougman, A., Nagaraj, N. & Mann, M. Universal sample preparation method for proteome analysis. *Nat. Methods* **6**, 359–362 (2009).
58. Rappsilber, J., Mann, M. & Ishihama, Y. Protocol for micro-purification, enrichment, pre-fractionation and storage of peptides for proteomics using StageTips. *Nat. Protoc.* **2**, 1896–1906 (2007).
59. Bruderer, R., Bernhardt, O. M., Gandhi, T. & Reiter, L. High-precision iRT prediction in the targeted analysis of data-independent acquisition and its impact on identification and quantitation. *Proteomics* **16**, 2246–2256 (2016).
60. Cox, J. et al. Accurate proteome-wide label-free quantification by delayed normalization and maximal peptide ratio extraction, termed MaxLFQ. *Mol. Cell. Proteomics* **13**, 2513–2526 (2014).

nature neuroscience

SUPPLEMENTARY INFORMATION

https://doi.org/10.1038/s41593-018-0296-9

In the format provided by the authors and unedited.

Loss of TREM2 function increases amyloid seeding but reduces plaque-associated ApoE

Samira Parhizkar[1], Thomas Arzberger[2,3,4,5], Matthias Brendel[6], Gernot Kleinberger[1,2], Maximilian Deussing[6], Carola Focke[6], Brigitte Nuscher[1], Monica Xiong[7], Alireza Ghasemigharagoz[8], Natalie Katzmarski[9], Susanne Krasemann[10,11], Stefan F. Lichtenthaler[2,3,12,13], Stephan A. Müller[3,12], Alessio Colombo[3], Laura Sebastian Monasor[3], Sabina Tahirovic[3], Jochen Herms[2,3,4], Michael Willem[1], Nadine Pettkus[1], Oleg Butovsky[10,14], Peter Bartenstein[2,6], Dieter Edbauer[2,3], Axel Rominger[2,6,17], Ali Ertürk[8], Stefan A. Grathwohl[15], Jonas J. Neher[15,16], David M. Holtzman[7], Melanie Meyer-Luehmann[9]* and Christian Haass[1,2,3]*

[1]Chair of Metabolic Biochemistry, Biomedical Center (BMC), Faculty of Medicine, Ludwig-Maximilians-Universität München, Munich, Germany. [2]Munich Cluster for Systems Neurology (SyNergy), Munich, Germany. [3]German Center for Neurodegenerative Diseases (DZNE) Munich, Munich, Germany. [4]Center for Neuropathology and Prion Research, Ludwig-Maximilians-Universität München, Munich, Germany. [5]Department of Psychiatry and Psychotherapy, Ludwig-Maximilians-Universität München, Munich, Germany. [6]Department of Nuclear Medicine, University Hospital, Ludwig-Maximilians-Universität München, Munich, Germany. [7]Department of Neurology, Hope Center for Neurological Disorders, and Charles F. and Joanne Knight Alzheimer's Disease Research Center, Washington University School of Medicine, St. Louis, MO, USA. [8]Institute for Stroke and Dementia Research, Klinikum der Universität München, Munich, Germany. [9]Department of Neurology, Medical Center University of Freiburg, and Faculty of Medicine, University of Freiburg, Freiburg, Germany. [10]Ann Romney Center for Neurologic Diseases, Department of Neurology, Brigham and Women´s Hospital, Harvard Medical School, Boston, MA, USA. [11]Institute of Neuropathology, University Medical Center Hamburg-Eppendorf, Hamburg, Germany. [12]Neuroproteomics, School of Medicine, Klinikum Rechts der Isar, Technische Universität München, Munich, Germany. [13]Institute for Advanced Study, Technische Universität München, Garching, Germany. [14]Evergrande Center for Immunologic Diseases, Brigham and Women's Hospital, Harvard Medical School, Boston, MA, USA. [15]Department of Cellular Neurology, Hertie Institute for Clinical Brain Research, University of Tübingen, Tübingen, Germany. [16]German Center for Neurodegenerative Diseases (DZNE) Tübingen, Tübingen, Germany. [17]Present address: Department of Nuclear Medicine, Inselspital, University Hospital Bern, Bern, Switzerland. *e-mail: melanie.meyer-luehmann@uniklinik-freiburg.de; christian.haass@mail03.med.uni-muenchen.de

Supplementary Figure 1

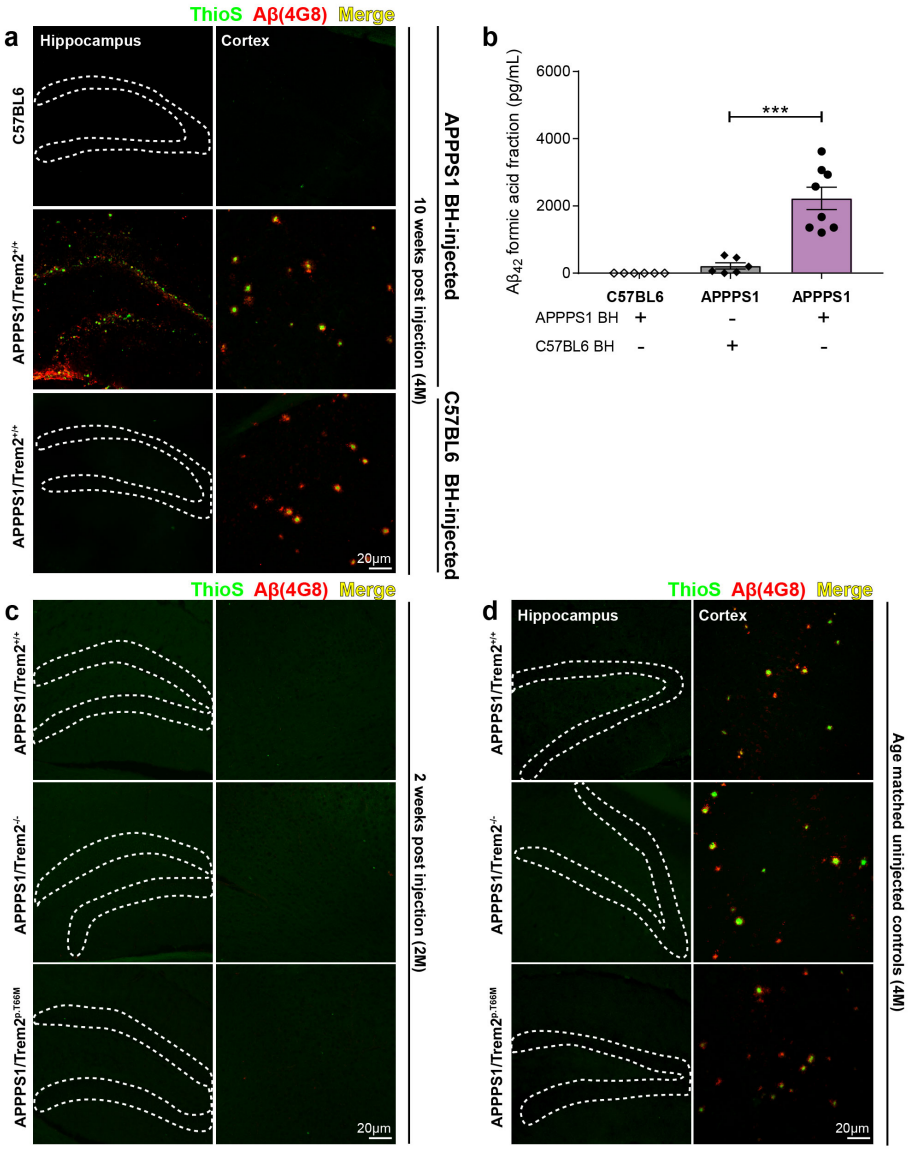

Supplementary Figure 1

Amyloid seeding occurs in a host-dependent manner.

a, Top: ThioS and 4G8 costaining for amyloid plaques in C57BL6 mice injected with APPPS1 brain homogenate (BH) (n=7 mice) show no plaques in the hippocampus or cortex ten weeks after injection. Middle: In contrast, amyloid seeding is induced in the hippocampus of APPPS1/Trem2$^{+/+}$ mice at four months (n=8 mice). Bottom: Age-matched C57BL6 brain homogenate-injected APPPS1 mice did not induce amyloid seeding in the hippocampus, although cortical plaques are present in the transgenic APPPS1 mice (n=6 mice). **b,** Quantification of $A\beta_{42}$ in formic acid fractions of C57BL6 brain homogenate-injected hippocampi by Meso-Scale discovery electrochemiluminescence assay confirm significantly lower plaque load compared to APPPS1 brain homogenate-injected hippocampi in APPPS1/Trem2$^{+/+}$ mice at four months. Data represent mean ± s.e.m. (APPPS1 BH-injected C57BL6 n = 6 mice, C57BL6 BH-injected APPPS1/Trem2$^{+/+}$ n=6 mice; APPPS1-injected APPPS1/Trem2$^{+/+}$ n = 8 mice; $F_{2,17}$ = 36.8, P = 1.1 × 10^{-5}). One-way ANOVA, Dunnett's *post hoc* analysis; ***P < 0.0001. **c,** APPPS1-brain homogenate injected APPPS1/Trem2$^{+/+}$, APPPS1/Trem2$^{-/-}$ and APPPS1/Trem2$^{p.T66M}$ mice show no hippocampal or cortical plaque staining two weeks after injection (n= 4 mice/genotype). **d,** Uninjected APPPS1/Trem2$^{+/+}$ mice show neither ThioS nor immunopositive amyloid plaques in hippocampus compared to cortex. Similar seeding patterns are not observed in the cortex because amyloid seeding is region-dependent[2] but note pre-existing non-experimentally seeded plaques within the cortex of four months old transgenic mice. Similarly, uninjected APPPS1/Trem2$^{-/-}$ and APPPS1/Trem2$^{p.T66M}$ mice show no ThioS or 4G8 positive plaques in the hippocampus compared to cortex (n=6 mice/genotype).

Supplementary Figure 2

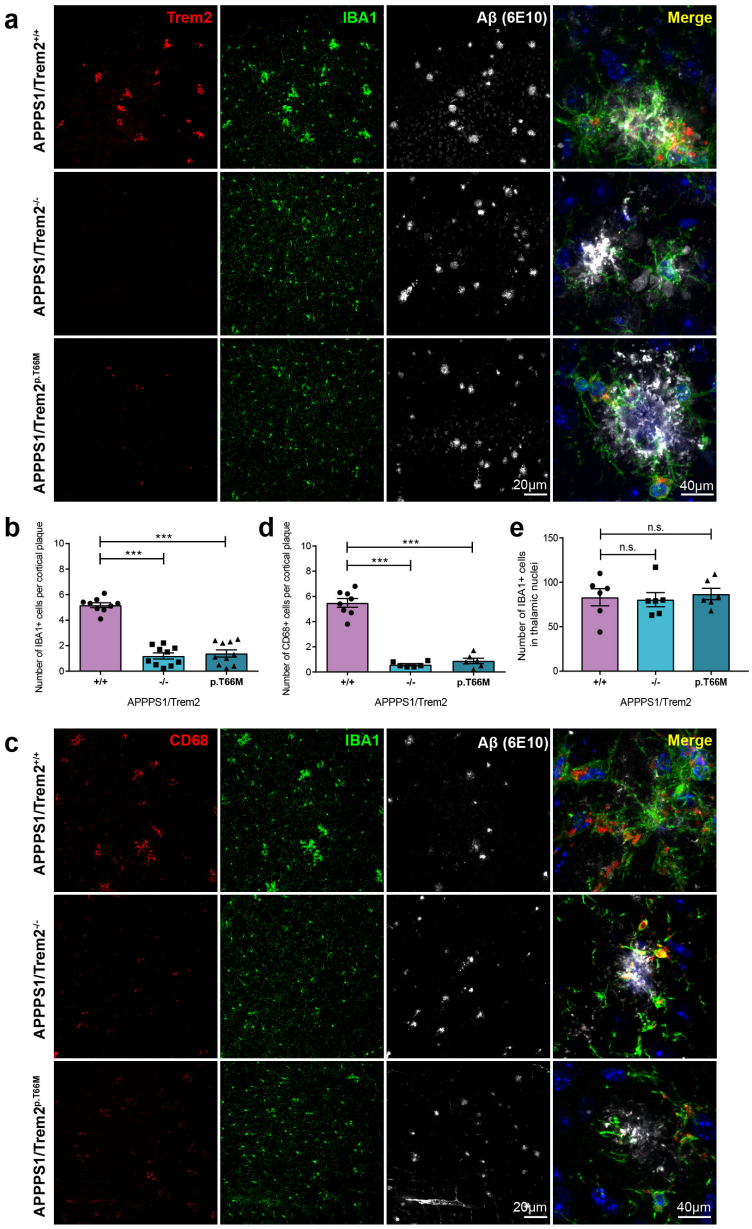

Supplementary Figure 2

Trem2 deficiency impairs microglial clustering and CD68 upregulation around cortical plaques.

a, APPPS1/Trem2$^{+/+}$ mice show increased microglia clustering around cortical plaques as compared to APPPS1/Trem2$^{-/-}$ and APPPS1/Trem2$^{p.T66M}$ mice. **b,** Number of IBA1-positive microglia cells quantified per plaque in the cortex ($n^{+/+}$ = 9 mice, $n^{-/-}$ = 10 mice, $n^{p.T66M}$ = 10 mice, $F_{2,26}$ = 83.07, P = 5.1 × 10^{-12}). **C,** APPPS1/Trem2$^{+/+}$ mice show increased CD68-positive microglia clustering around cortical plaques as compared to APPPS1/Trem2$^{-/-}$ and APPPS1/Trem2$^{p.T66M}$ mice. (**d**) Number of CD68-positive microglia cells quantified per plaque in the cortex ($n^{+/+}$ = 8 mice, $n^{-/-}$ = 6 mice, $n^{p.T66M}$ = 6 mice; $F_{2,17}$ = 109.7, P = 1.9 × 10^{-10}). (**e**) Number of IBA1-positive microglia cells quantified in plaque barren thalamic nuclei (n = 6 mice/genotype; $F_{2,15}$ = 0.1553, P = 0.8576). Data represent mean ± s.e.m. One-way ANOVA, Dunnett's *post hoc* analysis; n.s. P > 0.05; ***P < 0.0001.

Supplementary Figure 3

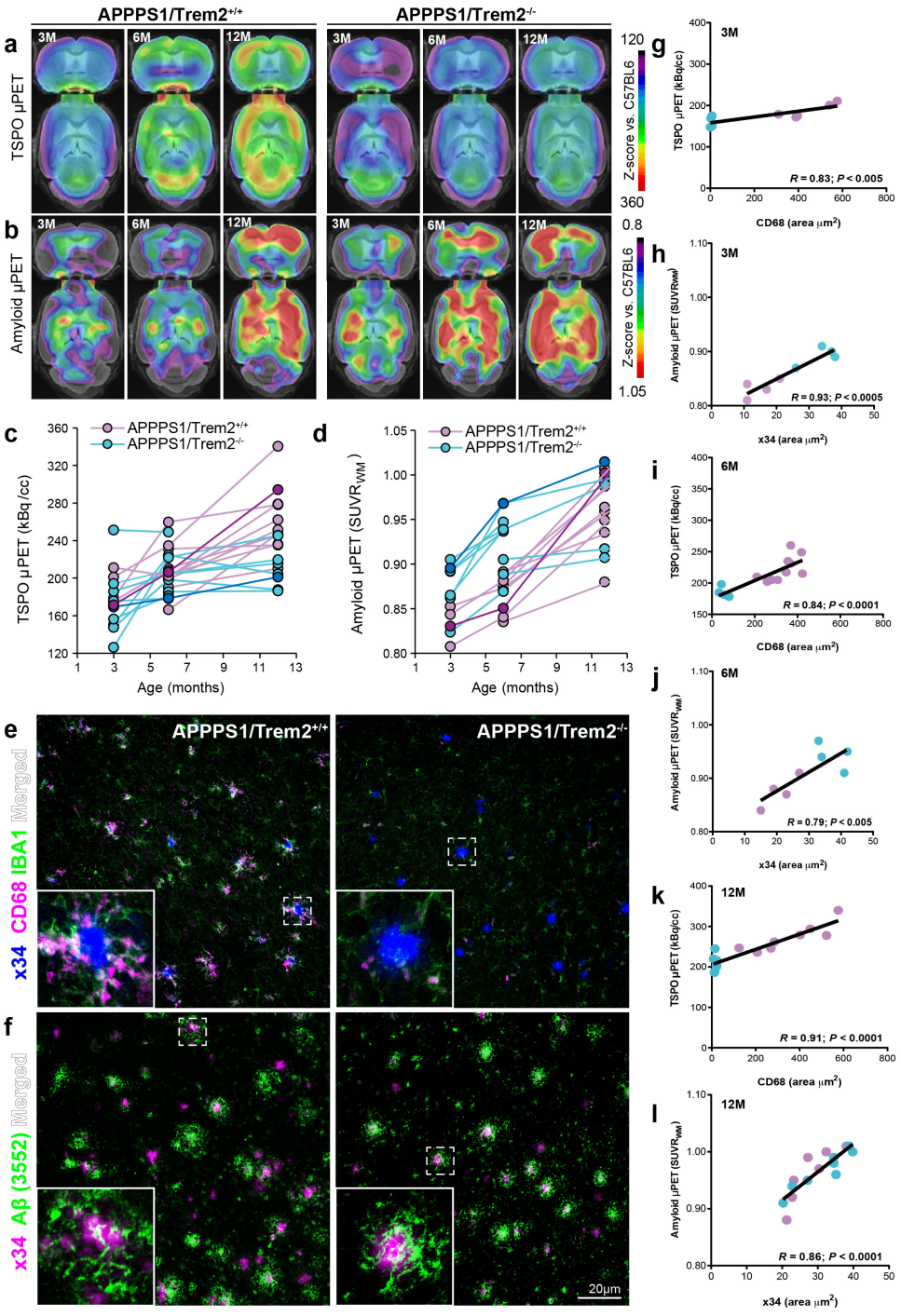

Supplementary Figure 3

Regression correlation analysis with longitudinal imaging of microglial activity as well as fibrillar amyloidogenesis in individual mice.

a,b, Coronal and axial slices show serial TSPO (**a**) and Amyloid µPET (**b**) Z-score increases (versus C57BL6) from three to twelve months of age for APPPS1/Trem2$^{+/+}$ and APPPS1/Trem2$^{-/-}$ mice. APPPS1/Trem2$^{-/-}$ mice indicate decreased microglial activity, most pronounced at twelve months of age, and higher fibrillar amyloidogenesis at three and six months of age when compared to APPPS1/Trem2$^{+/+}$ mice. **c,d,** Spaghetti plots show individual longitudinal time courses of cortical microglial activity (**c**) and fibrillar

amyloidogenesis (**d**) as assessed by *in vivo* µPET in APPPS1/Trem2$^{+/+}$ (purple highlighted data point corresponds to representative image shown in **e** and **f**) and APPPS1/Trem2$^{-/-}$ mice (dark blue highlighted data point corresponds to representative image shown in a and b). **e,f,** x34/CD68/IBA1 co-stained microglia ($n^{+/+}$ = 8 mice; $n^{-/-}$ = 7 mice) as well as (**e**) fibrillar and immunostained amyloid plaques (**f**) ($n^{+/+}$ = 8 mice; $n^{-/-}$ = 7 mice) of 12 months old APPPS1 mice previously included in longitudinal TSPO and Amyloid µPET imaging. **g,h,** Regression correlation analysis of CD68-positive phagocytic microglia staining and TSPO µPET imaging ($n^{+/+}$ = 5 mice, $n^{-/-}$ = 4 mice, P = 0.0026) (**g**) and x34-positive fibrillar Aβ staining and amyloid µPET imaging ($n^{+/+}$ = 4 mice, $n^{-/-}$ =4 mice, P = 0.0003) (**h**) in three months old APPPS1 mice. **i,j,** Regression correlation analysis of CD68 and TSPO µPET imaging ($n^{+/+}$ = 10 mice, $n^{-/-}$ = 5 mice, P = 5.2×10^{-5}) (**i**) and x34 and Amyloid µPET imaging ($n^{+/+}$ = 4 mice, $n^{-/-}$ =4 mice, P = 0.0088) (**j**) in six months old APPPS1 mice. **k,l,** Regression correlation analysis of CD68 and TSPO µPET imaging ($n^{+/+}$ = 8 mice, $n^{-/-}$ = 7 mice, P = 1.0×10^{-6}) (**k**) and x34 and Amyloid µPET imaging ($n^{+/+}$ = 7 mice, $n^{-/-}$ = 7 mice, P = 2.0×10^{-5}) (**l**) in 12 months old APPPS1 mice. Purple dots represent APPPS1/Trem2$^{+/+}$ and blue dots indicate APPPS1/Trem2$^{-/-}$ mice.

Supplementary Figure 4

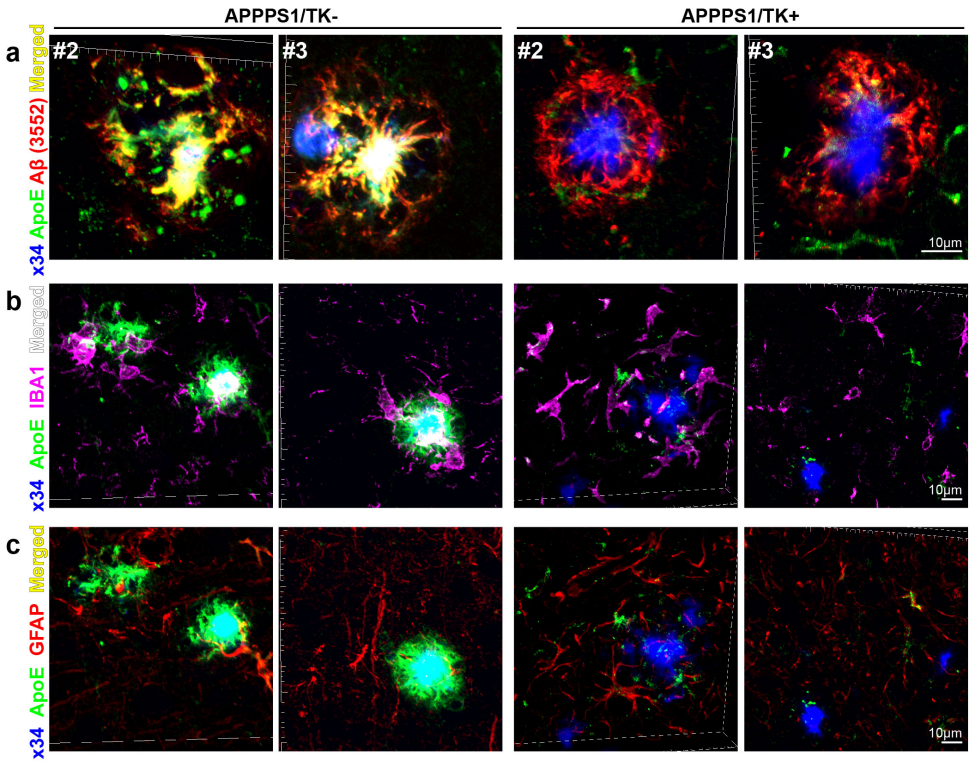

Supplementary Figure 4

Confocal images of individual microglia-depleted APPPS1/TK^{+} and control APPPS1/TK^{-} mice.

A, IMARIS 3D reconstructed high-resolution confocal images of x34/ApoE/Aβ stained cortical amyloid plaques of control APPPS1/TK- (left) and age matched microglia-depleted APPPS1/TK+ mice (right) (n=3 mice/genotype). Numbers at the top left of each image indicate three individual mice per group. **b,** Left: 3D reconstructed image of x34/ApoE/IBA1 staining shows higher ApoE and IBA1 colocalisation in APPPS1/TK- mice indicated by the degree of white merged staining, compared to; right: APPPS1/TK+ mice (n=3 mice/genotype). **c,** x34/ApoE/GFAP costaining in APPPS1/TK- mice looks comparable to APPPS1/TK+ mice (n=3 mice/genotype).

Supplementary Figure 5

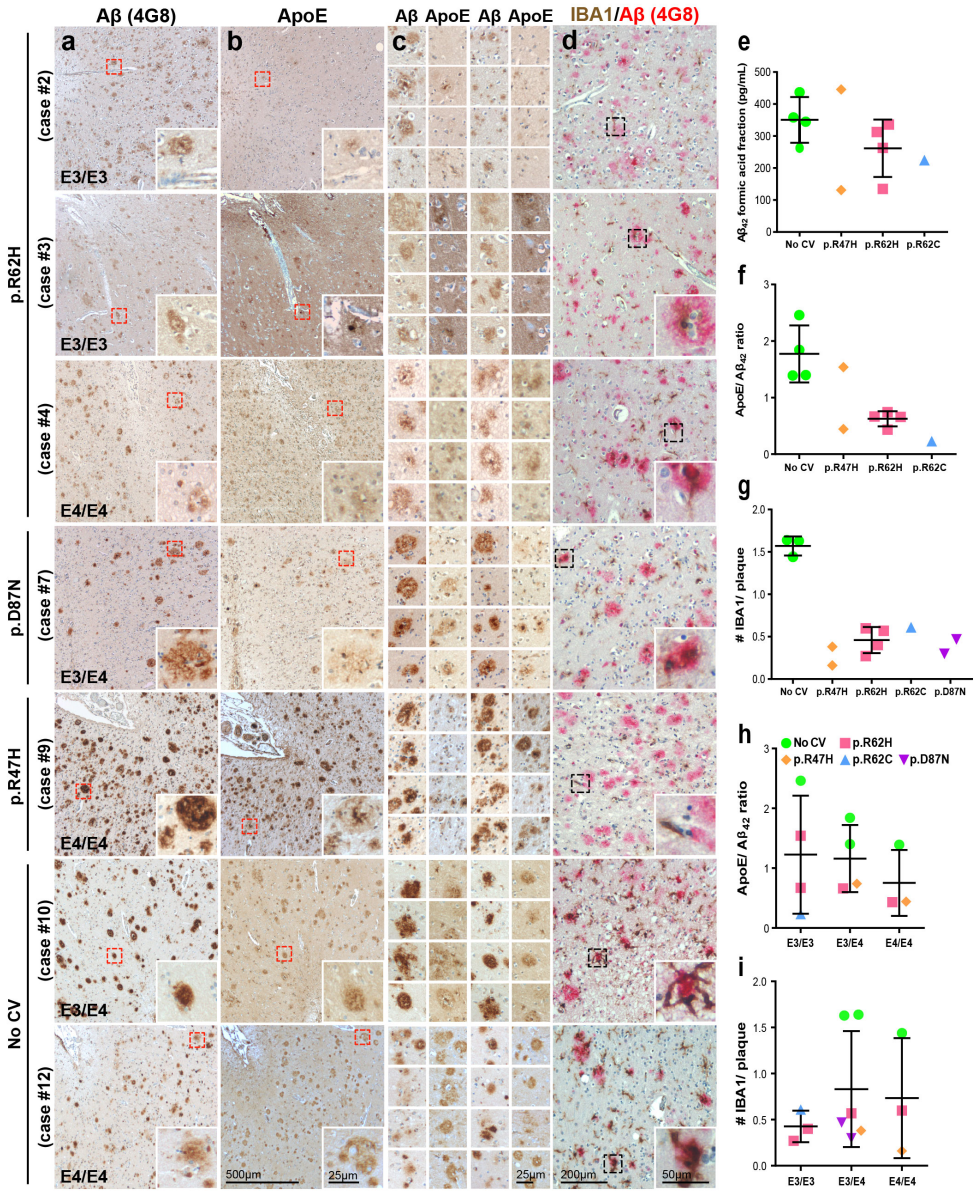

Supplementary Figure 5

Reduced ApoE levels in Aβ plaques and impaired microglial clustering in *TREM2* mutation carriers.

a, Temporal neocortex of additional human AD patients with and without the indicated examples of *TREM2* variants stained for Aβ by 4G8 immunohistochemistry. **b,** Reduced ApoE immunoreactivity within amyloid plaques compared to no CV shown in sections consecutive to those of the left column. Red boxes indicate the area in each staining that is magnified as inset. **c,** Additional examples of ApoE stainings comparing the same region in consecutive Aβ stained sections. **d,** Impaired clustering of microglial cells (brown) around and within amyloid plaques (red) in AD cases with different *TREM2* coding variants compared to no CV cases (last 2 rows). Dotted black boxes indicate the area magnified as inset. **e,** Quantification of $A\beta_{42}$ in formic acid fractions of temporal neocortex by Meso-Scale discovery electrochemiluminescence assay (n^{R47H} = 2 cases, n^{R62H} = 4 cases; n^{R62C} = 1 case; $n^{no\ CV}$ = 4 cases). **f,** ApoE/$A\beta_{42}$ ratio quantified from temporal neocortex plaque-enriched formic acid fraction (n^{R47H} = 2 cases, n^{R62H} = 4 cases; n^{R62C} = 1 case, $n^{no\ CV}$ = 4 cases). Of note, frozen material from p.D87N cases was not available and therefore not included. One of the no CV cases could not be included in the study due to diagnosed Hepatitis. **g,** Number of IBA1-positive microglia per plaque in temporal neocortex quantified from images shown in d and Fig. 8 (n^{R47H} = 2 cases, n^{R62H} = 4 cases; n^{R62C} = 1 case; n^{D87N} = 2 cases; $n^{no\ CV}$ = 3 cases). Noteworthy, sections from only three no CV cases were available in comparison to frozen material. No subjects were excluded

in this analysis. **h,** $A\beta_{42}$ in formic acid fractions quantified from temporal neocortex grouped according to *APOE* status ($n^{E3/E3}$ = 4 cases, $n^{E3/E4}$ = 4 cases; $n^{E4/E4}$ = 3 cases). **i,** Number of IBA1-positive microglia per plaque in temporal neocortex grouped according to *APOE* status ($n^{E3/E3}$ = 3 cases, $n^{E3/E4}$ = 6 cases; $n^{E4/E4}$ = 3 cases). Medial temporal cortex at the level of anterior hippocampus was used for all experiments. Data represent as mean ± s.d.

Supplementary Figure 6.

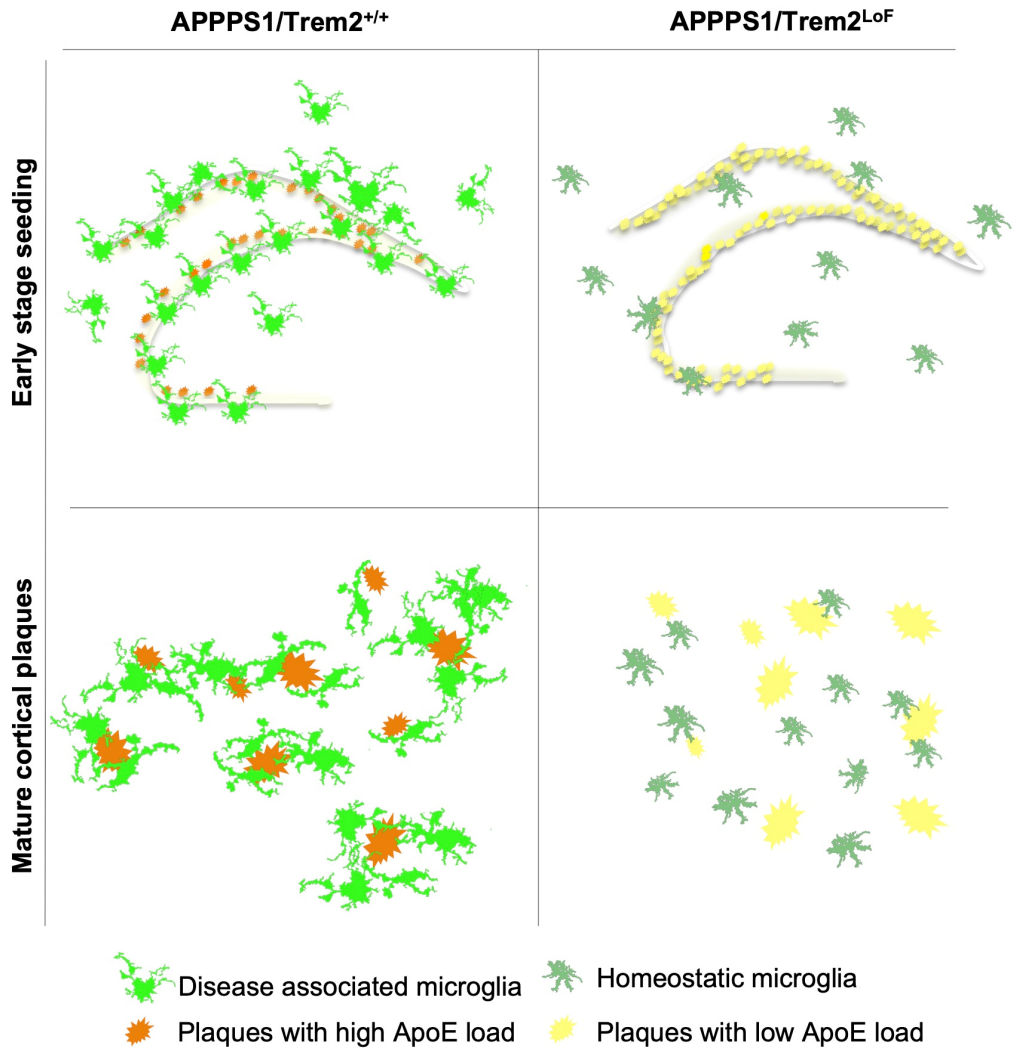

Supplementary Figure 6

Schematic summary.

Schematic figure of the consequences of a Trem2 loss-of-function (LoF) on microglial clustering and ApoE accumulation in amyloid plaques.

Supplementary Figure 7

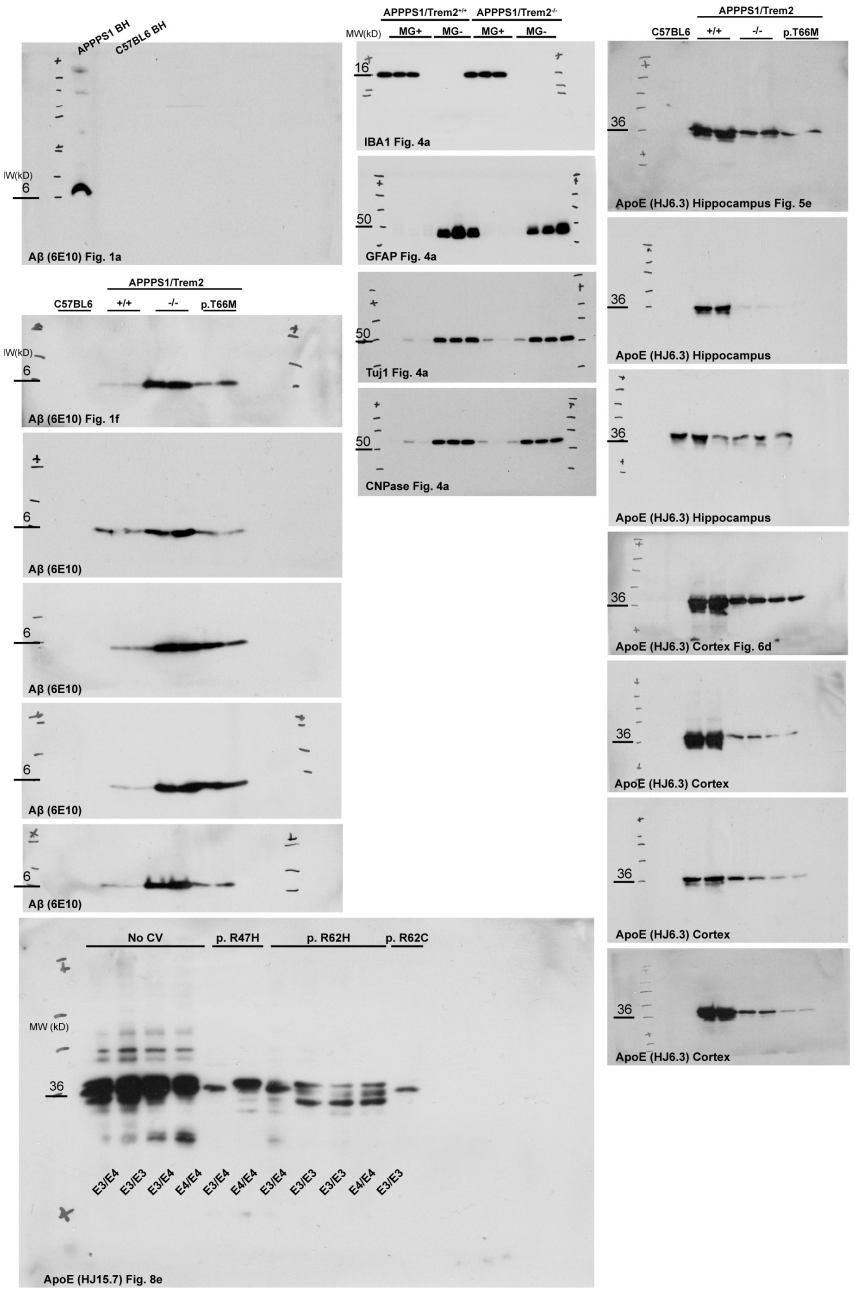

Supplementary Figure 7

Original western blots

Cropped KODAK films for Western blots in Fig. 1, Fig.4, Fig. 5, Fig. 6 and Fig. 8. Membranes were cut prior to antibody stainings to allow for detection of proteins running at different sizes on the same membrane.

Antigen	Type	Clone	Blocking serum /buffer	Primary antibody dilution	Source
IBA1	Rabbit polyclonal		Goat I-Block	1:500 IF 1:1000 IHC 1:1000 WB	Dako ThermoFisher
IBA1	Goat polyclonal		Donkey	1:500	Abcam
Trem2	Sheep polyclonal		Donkey	1:50	R&D Systems
GFAP	Goat polyclonal		Donkey	1:1000	ThermoFisher
GFAP	Rabbit polyclonal		I-Block	1:3000	Dako
Tuj1	Mouse monoclonal		I-Block	1:1000	Biolegend
CNPase	Mouse monoclonal		I-Block	1:1000	Abcam
Aβ1-16	Mouse monoclonal	6E10	Donkey I-Block	1:300 IF 1:2000 WB	Biolegend
Aβ17-24	Mouse monoclonal	4G8	Goat	1:1000 IF 1:4000 IHC	Biolegend
Aβ1-40	Rabbit monoclonal	3552	Donkey	1:2000	In-house antibody[6]
CD68	Rat monoclonal	FA-11	Goat	1:100	BioRad
Murine ApoE	Mouse monoclonal	HJ6.3/b	Donkey I-Block	1:300 IF 1:700 WB	D. Holtzman lab, Washington University [7]
Human ApoE	Mouse monoclonal	HJ15.7	Horse I-Block	1:3000 IHC 1:700 WB	D. Holtzman lab, Washington University [8]

Supplementary Table 1. List of antibodies used for experiments in mice and humans. IF – immunofluorescence staining; IHC – immunohistochemistry; WB-Western blot.

Case #	Brain bank	Clinical diagnosis	Age at death	Sex	Post mortem delay (days)	Braak & Braak AD stage	TREM2 variant	ApoE status	Thal phase Aβ	Modified CERAD	NIA classification
#1	Munich	Dementia, not specified	86	M	16-40	5	p.R62H	E3/E3	4	C	A3 B3 C3
#2	Munich	Dementia, not specified	81	F	n.i.	5	p.R62H	E3/E3	5	C	A3 B3 C3
#3	Munich	Dementia with rapid progression	75	M	24	6	p.R62H	E3/E4	5	C	A3 B3 C3
#4	Munich	Dementia Alzheimer type	78	F	21	6	p.R62H	E4/E4	5	C	A3 B3 C3
#5	Munich	Dementia frontotemporal	77	M	26	5	p.R62C	E3/E3	4	C	A3 B3 C3
#6	Munich	Dementia frontotemporal	78	M	5	5	p.D87N	E3/E4	5	C	A3 B3 C3
#7	UCL	Pick's Disease	71	M	40	6	p.D87N	E3/E4	5	C	A3 B3 C3
#8	UCL	Probable cortico-basal degeneration	64	M	36	6	p.R47H	E3/E4	5	C	A3 B3 C3
#9	UCL	AD	66	F	51	6	p.R47H	E4/E4	5	C	A3 B3 C3
#10	Munich	Dementia, Alzheimer type familial	62	F	132	6	None	E3/E4	5	C	A3 B3 C3
#11	Munich	Moderate dementia, probable Alzheimer type	82	M	15	6	None	E3/E4	5	C	A3 B3 C3
#12	Munich	Dementia Alzheimer type	93	F	n.i.	5	None	E4/E4	5	C	A3 B3 C3
#13	UCL	Young onset AD	64	F	76	6	None	E3/E3	5	C	A3 B3 C3
#14	UCL	AD (Logopenic Asphasia)	62	M	34	6	None	E3/E4	5	C	A3 B3 C3

Supplementary Table 2. Demographic and clinical characteristics of the control and TREM2 coding variant groups; n.i. – no information

nature research

Corresponding author(s): Melanie Meyer-Luehmann, Christian Haass

Reporting Summary

Nature Research wishes to improve the reproducibility of the work that we publish. This form provides structure for consistency and transparency in reporting. For further information on Nature Research policies, see Authors & Referees and the Editorial Policy Checklist.

Statistical parameters

When statistical analyses are reported, confirm that the following items are present in the relevant location (e.g. figure legend, table legend, main text, or Methods section).

n/a	Confirmed	
☐	☒	The exact sample size (*n*) for each experimental group/condition, given as a discrete number and unit of measurement
☐	☒	An indication of whether measurements were taken from distinct samples or whether the same sample was measured repeatedly
☐	☒	The statistical test(s) used AND whether they are one- or two-sided *Only common tests should be described solely by name; describe more complex techniques in the Methods section.*
☐	☒	A description of all covariates tested
☐	☒	A description of any assumptions or corrections, such as tests of normality and adjustment for multiple comparisons
☐	☒	A full description of the statistics including central tendency (e.g. means) or other basic estimates (e.g. regression coefficient) AND variation (e.g. standard deviation) or associated estimates of uncertainty (e.g. confidence intervals)
☐	☒	For null hypothesis testing, the test statistic (e.g. *F*, *t*, *r*) with confidence intervals, effect sizes, degrees of freedom and *P* value noted *Give P values as exact values whenever suitable.*
☒	☐	For Bayesian analysis, information on the choice of priors and Markov chain Monte Carlo settings
☒	☐	For hierarchical and complex designs, identification of the appropriate level for tests and full reporting of outcomes
☐	☒	Estimates of effect sizes (e.g. Cohen's *d*, Pearson's *r*), indicating how they were calculated
☐	☒	Clearly defined error bars *State explicitly what error bars represent (e.g. SD, SE, CI)*

Our web collection on statistics for biologists may be useful.

Software and code

Policy information about availability of computer code

Data collection	Confocal images were acquired using a LSM 710 Confocal microscope (Zeiss) and the ZEN 2011 software package (black edition, Zeiss). Stacks were 3D reconstructed using IMARIS 8 software.
Data analysis	FIJI (ImageJ) was used for all immunohistochemical analyses. Excel 2011 (Microsoft v14.7.7) was used to calculate the averages of each repeated experiment. Graph Pad (Prism v7.0) was used to build graphs and perform statistical analyses presented throughout the manuscript. All PET analyses were performed by PMOD (v3.4, PMOD technologies, Basel, Switzerland). Sequences for genotyping of AD cases were aligned to the TREM2 reference sequence (UCSC genome browser, assembly GRCh38/hg38; chr6:41,158,506-41,163,186) and variants called manually by two investigators using the CLC Main Workbench Software (Qiagen). Mass-spectrometry analysis and label free protein quantification were performed with the Spectronaut software (v11.0.15038.4.29119, Biognosys) and Maxquant (v1.5.5.1).

For manuscripts utilizing custom algorithms or software that are central to the research but not yet described in published literature, software must be made available to editors/reviewers upon request. We strongly encourage code deposition in a community repository (e.g. GitHub). See the Nature Research guidelines for submitting code & software for further information.

Data

Policy information about availability of data

All manuscripts must include a data availability statement. This statement should provide the following information, where applicable:

- Accession codes, unique identifiers, or web links for publicly available datasets
- A list of figures that have associated raw data
- A description of any restrictions on data availability

The data that support the findings of this study are available from the corresponding author upon request.

Field-specific reporting

Please select the best fit for your research. If you are not sure, read the appropriate sections before making your selection.

☒ Life sciences ☐ Behavioural & social sciences ☐ Ecological, evolutionary & environmental sciences

For a reference copy of the document with all sections, see nature.com/authors/policies/ReportingSummary-flat.pdf

Life sciences study design

All studies must disclose on these points even when the disclosure is negative.

Sample size	Although no power calculation was performed prior to study design, sample size was determined based on experience from previous findings (Meyer-Luehmann et al. Science 2006) including the success rate of intrahippocampal injections for amyloid seeding. Sample sizes for PET study was based on Brendel et al. 2017, Front Aging Neurosci, and Grathwohl et al. 2009 Nat Neurosci for microglia-depletion experiments. Sample size for human cases were based on availability. For micro-PET experiments, we aimed to include 8 mice per group to account for drop outs. A power of 0.8 at an alpha < 0.05 was estimated by N=6. All number of mice and AD cases analyzed are reported in the respective sections (i.e. Figure Legends, Online methods).
Data exclusions	Data exclusion criteria were pre-established before starting the seeding experiments such that data were excluded if intrahippocampal injections for amyloid seeding were unsuccessful. The number of mice per genotype were excluded as follows: APPPS1/Trem2+/+=4; APPPS1/Trem2-/-=3 and APPPS1/Trem2p.T66M=3. One of the control AD cases without TREM2 coding variant was diagnosed with Hepatitis and therefore excluded from experiments involving frozen brains.
Replication	For all IF, each staining was performed on at least 3 sections per mouse with 3 technical replicates. For quantification of IF images, around 10 images analyzed per animal. Quantification for mouse tissue was excluded if tissue folds were present or the quality of the staining was poor. Experiments on human samples were repeated at least twice. Moreover, we controlled for artifacts resulting from long formaldehyde fixation period by staining freshly fixed frozen tissue and comparing different antigen retrieval methods. Samples were measured in duplicates for amyloid beta ELISA. The key findings on Trem2 dependent ApoE loading of amyloid plaques was repeated independently in the labs of Oleg Butovsky and David Holtzman. Both came to the same conclusion. All attempts of replications were successful and each experiment was reproduced with similar results. Reproducibility has been either indicated in the Figure Legends, or shown as a quantification.
Randomization	For all animal experiments, mice were allocated randomly after genotyping. Mice of different genotype were allocated randomly to PET experiments (scan number and slot) and with blinded identity to the experimenter (chipping system). No randomization procedure was performed for selecting patient material as case inclusion was largely based on availability.
Blinding	S.P. was not blinded during the intrahippocampal injection experiments, however all immunohistochemical analysis was performed blinded. Immunohistochemical staining of human postmortem tissue was performed blinded and analysis of sections done by S.P. and T.A. For microglia counts, slides were imaged and saved with random numbers to identify them. Images were then quantified and unblinded to perform group statistics.

Reporting for specific materials, systems and methods

Materials & experimental systems

n/a	Involved in the study
☒	☐ Unique biological materials
☐	☒ Antibodies
☒	☐ Eukaryotic cell lines
☒	☐ Palaeontology
☐	☒ Animals and other organisms
☐	☒ Human research participants

Methods

n/a	Involved in the study
☒	☐ ChIP-seq
☒	☐ Flow cytometry
☒	☐ MRI-based neuroimaging

Antibodies

Antibodies used

IBA1 (1:1000, Thermo Fisher Scientific, catalog number #PA5-27436, RRID: AB_2544912); IBA1 (1:500 IF or 1:1000 IHC, Wako, catalog number #019-19741 RRID: AB_839504); IBA1 (1:500, Abcam, catalog number ab5076, RRID: AB_2224402); Trem2 (1:50, R&D systems, catalog number AF1729, RRID:AB_354956); GFAP (1:1000, Thermo Fisher Scientific, catalog number #PA5-18598, RRID:AB_10984384); GFAP (1:3000, Dako, catalog number #N1506, RRID:AB_10013482); TUJ1 (1:1000, BioLegend, catalog number #MMS-435P, RRID:AB_2313773; CNPase (1:1000, clone 11-5B, Abcam, catalog number #ab6319, RRID:AB_2082593); Aβ1-16 (1:300, clone 6E10, BioLegend catalog number #803013, RRID:AB_2564765); Aβ17-24 (1:1000 IF or 1:4000 IHC, clone 4G8, BioLegend, catalog number #800703, RRID:AB_662812); Aβ1-40 (1:2000, clone 3552 In-house (Page et al., 2010 J Biol Chem)); CD68 (1:100, clone FA-11, Bio-Rad/Serotec, catalog number #MCA1957T, RRID:AB_2074849); Murine ApoE (1:300IF or 1:700 WB, clone HJ6.3/b, Holtzman lab (Kim et al., 2012 JEM)); Human ApoE (1:3000 IHC or 1:700 WB, clone HJ15.7, Holtzman lab (Liao et al., 2015 Acta Neuropathol Comm)). For more information, please refer to supplementary table 1.

Validation

IBA1 (AB_2544912, AB_839504 and AB_2224402), Trem2 (AB_354956), GFAP (AB_10984384), GFAP (AB_10013482), TUJ1 (AB_2313773), CNPase (AB_2082593), Aβ1-16 (AB_2564765), Aβ17-24 (AB_662812), CD68 (AB_2074849) are verified for immunostaining and immunoblotting in mouse and human on the company websites.

Trem2 (AB_354956) was verified for immunostainings by Jay et al., 2015 JEM and Yuan et al., 2016 Neuron. Aβ1-40 (clone 3552) was validated in Page et al,. 2010 J Biol Chem as well as in McCarter et al., 2013 Acta Neuropathol, Bachhuber et al., 2015 Nature Medicine and Ziegler-Waldkirch et al., 2018 EMBO J for immunostainings in mice.
Murine ApoE (clone HJ6.3/b) was previously validated and published by the Holtzman lab (Kim et al., 2012 JEM) for mouse tissue and (clone HJ15.7) for human tissue (Liao et al., 2015 Acta Neuropathol Comm).

Specificity of Trem2 and ApoE antibodies were further tested and validated by using samples from the appropriate knock-out mouse line. Specificity of 3552 amyloid beta antibody was also tested on non-transgenic C57BL6 mouse tissue.

Animals and other organisms

Policy information about studies involving animals; ARRIVE guidelines recommended for reporting animal research

Laboratory animals

Seeding experiments:
4 months old male mus musculus APPPS1 (Thy1-APP695KM670/671NL; Thy-1PS1L166P) and age matched C57BL6 littermate controls were used. APPPS1 mice were crossed to TREM2-/- mice and maintained on a C57BL6J background. Additionally, APPPS1 were crossed to achieve homozygous TREM2 p.T66M knock-in mice (Kleinberger et al 2016, EMBO Journal), which were maintained on a mixed genetic background (N1 backcross to C57BL/6N). The TREM2 p.T66M mice were compared to APPPS1/TREM2 wild-type mice from the same background for all experiments.

Micro-PET experiments:
3, 6 and 12 months old female APPPS1/TREM2+/+ and age matched APPPS1/TREM2-/- were used. Additionally age, gender and genotype matched C57BL6 controls were also used.

Microglia isolation experiments:
Microglia were isolated from 3, 6 and 12 months old APPPS1 and age matched C57BL6 controls. Additionally, ApoE protein expression was performed on 12months old APPPS1/TREM2-/- mice with age matched APPPS1 controls. Both males and females were used for these experiments.

Microglia depletion experiments:
4 months old male APPPS1 mice crossed to HSTK expressing mice and treated with ganciclovir for two weeks for microglia depletion (Grathwohl et al. 2009, Nature Neuroscience). Additionally age and gender matched APPPS1 mice were used as controls.

Wild animals

No wild animals were used in this study.

Field-collected samples

No field-collected samples were used in this study.

Human research participants

Policy information about studies involving human research participants

Population characteristics	No living patients participated in this study. The patient characteristics for the postmortem samples included in this study are detailed in Online Methods and Supplementary Table 2. Case #1, Brain bank Munich, Clinical diagnosis: Dementia, not specified, 86 years old, Male, Post mortem delay 16-40 days, Braak & Braak AD stage 5, TREM2 variant p.R62H, ApoE E3/E3, Thal Phase 4, CERAD C, NIA classification A3 B3 C3 Case #2 Brain bank Munich, Clinical diagnosis: Dementia, not specified, 81 years old, Female, Post mortem delay information not available, Braak & Braak AD stage 5, TREM2 variant p.R62H, ApoE E3/E3, Thal Phase 5, CERAD C, NIA classification A3 B3 C3 Case #3, Brain Bank Munich, Diagnosis: Dementia with rapid progression, 75 years old, Male, Post mortem delay 24 days, Braak and Braak AD stage 6, TREM2 variant p.R62H, ApoE E3/E4, Thal Phase 5, CERAD C, NIA classifiation A3 B3 C3 Case #4, Brain Bank Munich, Diagnosis: Dementia Alzheimer type, 78 years old, Female, Post mortem delay 21 days, Braak and Braak AD stage 6, TREM2 variant p.R62H, ApoE E4/E4, Thal Phase 5, CERAD C, NIA classification A3 B3 C3 Case #5, Brain Bank Munich, Diagnosis: Dementia frontotemporal, 77 years old, Male, Post mortem delay 26 days, Braak and Braak AD stage 5, TREM2 variant p.R62C, ApoE E3/E3, Thal Phase 4, CERAD C, NIA classification A3 B3 C3 Case #6, Brain Bank Munich, Diagnosis: Dementia frontotemporal, 78 years old, Male, Post mortem delay 5 days, Braak and Braak AD stage 5, TREM2 variant p.D87N, ApoE E3/E4, Thal Phase 5, CERAD C, NIA classification A3 B3 C3 Case #7, Brain Bank UCL, Diagnosis: Pick's Disease, 71 years old, Male, Post mortem delay 40 days, Braak and Braak AD stage 6, TREM2 variant p.D87N, ApoE E3/E4, Thal Phase 5, CERAD C, NIA classficiation A3 B3 C3 Case #8, Brain Bank UCL, Diagnosis: Probable cortico-basal degeneration, 64 years old, Male, Post mortem delay 36 days, Braak and Braak AD stage 6, TREM2 variant p.R47H, ApoE E3/E4, Thal Phase 5, CERAD C, NIA classification A3 B3 C3 Case #9, Brain Bank UCL, Diagnosis: AD, 66 years old, Female, Post mortem delay 51 days, Braak and Braak AD stage 6, TREM2 variant p.R47H, ApoE E4/E4, Thal Phase 5, CERAD C, NIA classification A3 B3 C3 Case #10, Brain Bank Munich, Diagnosis: Dementia, Alzheimer type familial, 62 years old, Female, Post mortem delay 132 days, Braak and Braak AD stage 6, TREM2 variant None, ApoE E3/E4, Thal Phase 5, CERAD C, NIA classification A3 B3 C3 Case #11, Brain Bank Munich, Diagnosis: Moderate dementia, probable Alzheimer type, 82 years old, Male, Post mortem delay 15 days, Braak and Braak AD stage 6, TREM2 variant None, ApoE E3/E4, Thal Phase 5, CERAD C, NIA classification A3 B3 C3 Case #12, Brain Bank Munich, Diagnosis: Dementia Alzheimer type, 93 years old, Female, Post mortem delay information not available, Braak and Braak stage 5, TREM2 variant None, ApoE E4/E4, Thal Phase 5, CERAD C, NIA classification A3 B3 C3 Case #13, Brain Bank UCL, Diagnosis: Young onset AD, 64 years old, Female, Post mortem delay 76 days, Braak and Braak AD stage 6, TREM2 variant None, ApoE E3/E3, Thal Phase 5, CERAD C, NIA classification A3 B3 C3 Case #14, Brain Bank UCL, Diagnosis: AD (Logopenic Asphasia), 62 years old, Male, Post mortem delay 34 days, Braak and Braak AD stage 6, TREM2 variant None, ApoE E3/E4, Thal Phase 5, CERAD C, NIA classification A3 B3 C3
Recruitment	All patient material was obtained from people who had enrolled in the brain donation program while still alive. All material collection procedures were approved by the ethical committee. Therefore no investigator bias was present that could impact results.